Effects of the electric field on soot formation in combustion: A coupled charged particle PBE-CFD framework

Anxiong Liu[a], Kai H. Luo[a,*], Stelios Rigopoulos[b], William Jones[b]

[a]*Department of Mechanical Engineering, University College London, London WC1E 7JE, United Kingdom*
[b]*Department of Mechanical Engineering, Imperial College London, London SW7 2AZ, United Kingdom*

Abstract

In this article, a coupled PBE-CFD framework has been proposed to study counterflow non-premixed flames and soot formation under an external electric field. This framework integrates the population balance equation (PBE) for nanoparticle dynamics into an in-house CFD solver for the multicomponent reactive flows. Different electric properties have been considered in this model. An ion mechanism used in both fuel-rich and fuel-lean combustion is combined with a detailed chemistry for neutral gaseous species and small-size aromatics to retain the full chemistry. In order to model soot particles carrying charges and the movement of the reacting fluid medium in the electric field, a second PBE for the production and transport of charges on soot particles is introduced for the first time and incorporated into the original PBE for the number density of particles. Also, the electric force for the gas mixture is included in the momentum equations. The electric drift velocities for ions and soot particles are also considered in the transport equations of ions and the PBE of soot particles, respectively.

The simulations have shown that the presence of the electric field modifies the stagnation plane of the counterflow flames and reduces the soot formation in both rich-fuel and lean-fuel conditions in agreement with experimental observations. The application of the soot particle charging model, accompanied by a proper electric correction factor on the nanoparticle processes of nucleation and surface growth, significantly improves the stability of the flame structure. The introduction of the electric correction factor reveals that the suppression of soot formation in an electric field is mainly caused by the inhibited chemical reactions of the PAH nucleation and particle surface growth, which is more important than the electric drift of the charged particles. Reducing the critical size of the particle charging process enhances the electric drift of nascent soot, thus lessening its subsequent evolution.

Keywords: electric field, non-premixed flames, soot formation, nanoparticle charging, population balance equation

1. Introduction

Electric fields or plasma-assisted combustion can be a viable option for combustion control. In an effort to develop an advanced combustion system with high energy efficiency, improved flame stability and reduced pollutant emissions,

*Corresponding author
Email address: k.luo@ucl.ac.uk (Kai H. Luo)

the influence of an external electric field on the behaviours of premixed and diffusion flames has been extensively investigated. For example, electric fields have been found to cause slight deceleration [1], slight acceleration [2, 3] and strong acceleration of up to 200% [4, 5] in different experiments. Moreover, the external electric fields have been observed to extend the combustion stability by preventing or controlling the liftoff [6, 7] or blowoff [8–11] in premixed [12] and non-premixed flame [13] flames.

Three different mechanisms have been postulated in the literature to explain the effect of the electric field on flames: ionic wind, ohmic heating and kinetic enhancement by non-thermal electrons [14]. Flames are under weakly ionised plasma states since charged particles (like H_3O^+, HCO^+, $C_3H_3^+$ and electrons, e^-) are generated in the reaction zones through chemionisation and subsequent ion chemistry. Under an external electric field, the charged particles are accelerated by the electric forces. Collisions between charged particles and neutral molecules result in momentum and energy changes in the reacting mixture. The infusion of momentum causes the bulk flow to drift in a macroscopic form of an ionic wind. On the other hand, the energy addition leads to an increase of temperature, similar to the ohmic heating in a conductor with the current passing through, thus enhancing the reactivity of the mixture. The ohmic heating is usually overshadowed by the exothermic chemical reactions in the flames, except when the background electric intensity or alternating accurency (AC) frequency is extremely high. For example, the spark plug in gasoline engines introduces a strong electrical field to ionise and thus build a time circuit (spark) in the air-fuel mixture, igniting the chemical reactions with intensive ohmic heat [15]. Another example is the high-frequency (GHz) microwave ignition. This technique has been used in internal combustion engines (ICE) [16] and combustion synthesis of nanoparticles [17, 18]. As the mass of electrons is much smaller than that of other ions, the electrons can be accelerated with much higher velocity /energy in the electric field. These non-thermal electrons later transfer energy to neutral molecules and ions, contributing an additional source of chain ionisation reactions [19, 20].

The effects on soot emissions when flames are exposed to external electric fields have also been studied in a number of experiments [21–25]. Saito et al. [26] and Park et al. [24] showed a reduction of 90% in the soot formation in an acetylene co-flow flame under the action of an axial DC electric field. Park et al. [24] discovered that no noticeable sooting limit is found by varying the ethylene (oxygen) mole fraction in an ethylene counterflow flame subject to an axial electric field. In an AC electric field, the sooting zone of a laminar diffusion flame becomes narrower in width and height as the electrical voltage increases. For the soot morphology, Wang et al. [27] identified that in a laminar premixed ethylene flame, the fractal shape of an agglomerate depends on the field intensity while the primary particle size does not change. However, Sayed-Kassem et al. [28] found that in a laminar diffusion flame, the soot volume fraction (SVF) diminishes and the average primary particle diameter slightly increases when an electric field is applied. The main explanation is that the ionic wind-driven flow field reduces the flow residence time and increases the temperature field, which are important factors for the formation and growth of soot [24, 28]. In addition, the soot precursors and particles are charged under the electric field, which modifies the reaction path of soot formation and the aggregation of primary particles [29]. As an application, the Scanning Mobility Particle Sizer (SMPS) is a device to measure the particle size distribution of aerosols or soot [30], based on the principle that a particle is charged in an

electric field and of a certain drift mobility with respect to its size.

Modelling approaches have also been developed to predict the combustion in the presence of an external electric field. Many studies have employed the framework of computational fluid dynamics (CFD) to account for the following effects: the electric intensity induced by the external electric field and the electrostatic field of ions, the electrostatic force exerting on the fluid, an additional drift velocity of ions and the ohmic heating [31–37]. The simulations have been performed for one/two-dimensional co-flow flames, counterflow flames and premixed flames subject to DC/AC electric field. These simulations have confirmed the existence of the ion-driven winds, showing that the flame structure [32], flame stability [33] and [37] propagation speed can be modulated in the presence of an electric field.

However, simulations of flames with soot formation subject to an electric field have not been reported. Three challenges need to be addressed for this objective to be realised. First of all, the reacting flow, the electrostatic field and the soot formation should be properly coupled. Even in the existing studies of coupling the reacting flow with the electrostatic field only, significant challenges appear. For example, mobility of electrons in the electric field is much speedier than ions, which leads to a very short time step (10^{-9}- 10^{-7}s) [34]. Also, the coefficients of diffusion and mobility of electrons and ions are usually not approximated consistently in the literature [38]. Second, a number of inconsistencies still exist in the soot formation modelling (see the discussions in [39, 40]). For example, both the acetylene-based nucleation and the PAH-based nucleation are widely used in the modelling. The surface growth rates vary based on the chemical mechanisms. Moreover, the diversity of numerical approaches [41] of solving soot formation (*i.e.*, the methods of moments, the discretised population balance modelling, the Monte Carlo-type method) lead to different treatments when coupling with the electrostatic field. Third, soot particles are charged subject to an electric field, leading to extra effects on the reacting flow medium and the evolution processes of soot formation. For example, the charges on soot particles influence the local electrostatic field and contribute to the ionic wind, also modulating the spatial distribution of soot. In the meantime, the electric repulsive force between the charged particles will slow down the coagulation and aggregation process of soot.

The objective of the present work is to propose a new framework that describes the interactions among the reacting flow, the electrostatic field and the soot formation. To the authors' knowledge, this is the first attempt reported in the literature to numerically investigate a multi-dimensional sooting flame subject to an electric field. In particular, we formulate a two-equation population balance equation (PBE) to account for the distributions of the particle size and charges on particles, respectively. The spatial motion and temporal evolution of charged soot particles can thus be evaluated, with the combined effects of transport phenomena, chemical processes and electric forces. This model is validated against experimental data in ethylene counterflow diffusion flames by [24]. The numerical simulations also provide insights for understanding the experimental measurements.

2. Numerical Framework for Ionic Reacting Flows

In this section, the governing equations for compressible, gaseous multi-component, reacting flow in the presence of electric body forces are formulated. The dataset of ionic / chemical reactions and the thermophysical properties for the gas-phase ions / species are introduced. Finally, the numerical framework proposed for ionic reactive flows is applied to a counterflow flame subject to the electric field [24].

2.1. Reacting flow in an electric field

Under the direct-current electric field, the electrostatics properties can be fully determined by Poisson's equation (one of Maxwell's equations), which relates the electric scalar potential Φ to the concentrations of ions, electrons and charged particles. The electric potential must be updated at each time step as the charges evolve in the electric field over time:

$$\nabla^2\Phi = -\frac{e(C^+ - C^-)}{\epsilon_0} \tag{1}$$

where C^+ and C^- are the number of positive and negative charges in the unit spatial volume, respectively. These are dependent on the ionic space density and charges on soot particles,

$$C^+ - C^- = \left[\rho N_\mathrm{A} \sum_k \frac{S^k Y_k}{W_k} + \int N_\mathrm{c}(v)\mathrm{d}v\right] \tag{2}$$

e and ϵ_0 represent the unit charge (1.60 $\times 10^{-19}$ C) and the permittivity of free space (8.854 $\times 10^{12}$ $\mathrm{C}^2 \cdot \mathrm{s}^2/\mathrm{kg}$), respectively. ρ is the density of the gas mixture and N_A is the Avogadro constant. Y_k is the mass fraction of a neutral or ionic species in the gas mixture. W_k and S_k express the molecular weight and the number of positive charges of an ion or electron with a negative sign, respectively. N_c [C / $\cdot \mathrm{m}^3 \cdot \mathrm{m}^3$] is the charge of particles in the unit volume and the unit particle size v.

The components of the electric field intensity E_i are related to the spatial derivatives of electric potential Φ,

$$E_i = -\frac{\partial \Phi}{\partial x_i} \tag{3}$$

The Navier Stokes equations including electric body forces are expressed in the Cartesian tensor form as follows:

$$\frac{\partial \rho}{\partial t} + \frac{\partial \rho u_i}{\partial x_i} = 0 \tag{4}$$

$$\frac{\partial \rho u_j}{\partial t} + \frac{\partial \rho u_i u_j}{\partial x_i} = -\frac{\partial p}{\partial x_j} + \frac{\partial \tau_{ij}}{\partial x_i} + F_j \tag{5}$$

where t and x_i are the time and space coordinates, correspondingly. p is the static pressure calculated by the ideal gas equation and τ_{ij} is the viscous tensor for Newtonian fluids. The components of the electric body force F_i exerted on

the fluid are defined as ,

$$F_j = eE_j(C^+ - C^-) \tag{6}$$

The transport equations for neutral and charged species are uniformly expressed as,

$$\frac{\partial \rho Y^k}{\partial t} + \frac{\partial \rho u_i Y^k}{\partial x_i} = -\frac{\partial Y^k V_i^k}{\partial x_i} + \dot{\omega_k} \tag{7}$$

where V_i^k is the i-component of the diffusion velocity of species k (representing a neutral molecule, an ion or an electron). In the mixture-average formulation, the diffusion velocity is due to the gradient of the species concentration by the Fickian law and the thermophoresis effect [42], neglecting the effect of pressure gradients for flames in the open air,

$$V_{k,i} = -\frac{1}{X_k} D_{km} \frac{\partial X^k}{\partial x_i} - D_k^{\mathrm{T}} \frac{\partial (\ln T)}{\partial x_i} \tag{8}$$

For charged species, the electrical mobility (electrophoresis) [43] is added to the diffusion velocity,

$$V_{k,i} = -\frac{1}{X_k} D_{km} \frac{\partial X^k}{\partial x_i} - D_k^{\mathrm{T}} \frac{\partial (\ln T)}{\partial x_i} + S^k \mu^k E_i \tag{9}$$

The coefficients of mass diffusion D_{km}, thermal diffusion D_k^{T} and electrophoresis μ^k will be discussed in Section. 3. The chemical source terms $\dot{\omega}_k$ are given by the Arrhenius law for the specified chemical mechanism.

The energy equation in terms of total enthalpy (standard enthalpy of formation plus sensible enthalpy) is solved to obtain the temperature field which determines the chemical reaction rates,

$$\frac{\partial H}{\partial t} + \frac{\partial u_i H}{\partial t} = -\frac{\partial q_i}{\partial x_i} + \dot{Q} + f_{\mathrm{E}} \tag{10}$$

where the terms q_i, $\dot{Q}$ and f_{E} are the energy flux inside the fluid, the external heat addition and the work by the electric force, respectively. In the laminar diffusion flame at low Mach number, the work by the gravity force, the viscous stress and the pressure is all neglected. The energy flux contains the contributions resulting from the inter-diffusion of various substances and thermal conductive flux and the Dufour effect,

$$q_i = \sum_k \rho Y_k V_{k,i} h_k - \lambda \frac{\partial T}{\partial x_i} - \sum_k \frac{RT}{w_k X_k} D_k^{\mathrm{T}} - \frac{\partial X_k}{\partial x_i} \tag{11}$$

where h_k is the specific enthalpy of species k. In order to account for the radiation in mixture enthalpy $\dot{Q}$, we use a radiation model based on the assumption of optical thinness [44]. This model accounts for radiation of water vapour, CO_2, CH_4, CO, N_2 and soot particles. The energy source by the electric force is given by:

$$f_{\mathrm{E}} = \sum_k e \frac{\rho Y_k}{W_k} S_k E_i \left(u_i + V_{k,i}\right) \tag{12}$$

It should be noted that the momentum, species and energy equations (Eqs. 5, 7 and 10) all include an electric potential term. The only governing equation that does not have an explicit term of the electric field is the mass conservation equation (Eq. 4). The above modelling framework has been implemented in a reactive flow solver BOFFIN for the multi-component ideal gases, to investigate the electric field effects.

2.2. Chemical / ionic reactions and transport properties

The chemical reactions are adopted from [45], involving 149 species and 928 reactions. This mechanism is developed based on the GRI 3.0 mechanism, including the chemistry of soot precursors such as acetylene, C_3H_4 isomers and benzenel. It also accounts for all major pathways of PAH formation up to pyrene ($C_{16}H_{10}$) and cyclopentapyrene ($C_{18}H_{10}$). This mechanism has been validated for the combustion of many fuels ranging from methane to iso-octane and one-ring aromatics in various configurations like homogeneous auto-ignition, laminar premixed flames and diffusion flames. With its emphasis on soot precusors, this mechanism has been used in modelling soot inception and growth in laminar ethylene diffusion flames [40].

Chen et al. [29] proposed an updated ion chemistry which can be used in both fuel-rich and fuel-lean combustion, based on the assembled ion mechanism by Prager et al. [46]. The new mechanism contains six cations (H_3O^+ , CH_3^+, HCO^+, CH_5O^+, $C_2H_3O^+$ and $C_3H_3^+$), six anions (O_2^-, OO, OHOH, CHO_2CHO_2, CHO_3CHO_3 and CO_3CO_3) and electron e, and 86 elementary ion reactions in total. It is widely known that H_3O^+ is the dominant cation in lean and stoichiometic flames, but Jones and Hayhurst [47] measured that the amount of $C_3H_3^+$ became significant in rich flames ($\phi > 1.8$), which has been neglected in previous mechanisms [33, 35, 46].

The thermodynamic and transport properties of the species and ions are obtained from the sources by Blanquart et al. [45] and Chen et al. [29] respectively. A mixture-averaged diffusion coefficient $D_{k\mathrm{m}}$ for each species k is employed [48] . Particularly, the mass diffusive coefficient for electrons D^{e} is approximated by Delcroix [49], referred in many modelling research [33, 50], as

$$D^{\mathrm{e}} = \left(\frac{m^{\mathrm{i}}}{m^{\mathrm{e}}}\right)^{0.5} D^{\mathrm{i}} \tag{13}$$

where m^{e} represents the electron mass and m^{i} is the mole fraction weighted mass of an ion. D^{i} is the mole fraction weighted diffusion coefficient of ions. The electric mobility coefficients for ions and electrons are important as the electric current at any point in a flame is proportional to the product of the local values of mobility and ion number density. The electric mobility also affects the spatial distribution of ions and electrons subject to an external electric field, thus modulating the local electric field intensity. In fact, the rigorous calculation of electrical mobility properties should be based on quantum mechanism. For example, the electron transport properties must be computed starting from collision cross sections of electron/neutral pair. Conversely, the ion transport properties should be calculated by the (n,6,4)-potential for the ion/neutral interaction, and the Debye–Hückel potential for the interaction between two ions. However, this treatment is very expensive in the application of plasma fluid models in combustion, which are hetergeneous in temperature and composition. Routinely , numerical simulations of plasma flames rely on simplified

treatments of electric mobility coefficients [51]. Table 1 summarised the values of electrical mobility recommended and commonly used in the literature.

Han et al. [50] studied the impact of the choice of electron mobility on the ion distributions in a freely propagating premixed lean CH4/O2 flame and found that the profiles of charged species as well as their maximum total densities and net fluxes are not affected significantly (less than 4 %) by changing the electron mobility in the range of 0.2-0.6 $\mathrm{m}^2/(\mathrm{V}\cdot\mathrm{s})$ or using the following assumption,

$$\mu_\mathrm{e} = \left(\frac{m_\mathrm{i}}{m_\mathrm{e}}\right)^{0.5} \mu_\mathrm{i} \tag{14}$$

Therefore, in this work, we have not focused on the effect of the electric mobility of ions and electrons on the flame. In the following simulations, we apply the models of electric mobilities of ions, electrons and soot particles on the first line of Table 1.

Ions		**Electrons**		**Soot**	
References	Values	References	Values	References	Values
[33, 52]	$1.0\times10^{-4}\mathrm{m}^2/(\mathrm{V}\cdot\mathrm{s})$	[33, 50]	$\mu_\mathrm{e} = \left(\frac{m_\mathrm{i}}{m_\mathrm{e}}\right)^{0.5}\mu_\mathrm{i}$	[53]	$\mu_\mathrm{p} = \frac{qD_\mathrm{p}}{k_\mathrm{B}T}$
[31, 54]	$2.9\times10^{-4}\mathrm{m}^2/(\mathrm{V}\cdot\mathrm{s})$	[38]	$\mu_\mathrm{e} = \frac{2\mathrm{e}}{3\tilde{\sigma}_\mathrm{m}p}\sqrt{\frac{2\mathrm{e}T}{\pi m_\mathrm{e}}}$		
[55]	$1.7\times10^{-4}\mathrm{m}^2/(\mathrm{V}\cdot\mathrm{s})$	[50]	$0.2-0.6\mathrm{m}^2/(\mathrm{V}\cdot\mathrm{s})$		
[53]	$\mu_\mathrm{i} = \frac{qD_\mathrm{i}}{k_\mathrm{B}T}$				

Table 1: Widely used models of electrical mobility coefficients for ions / electrons

2.3. Simulation cases: Counterflow diffusion laminar flames under DC electric fields

In order to validate the modelling framework described above, an experimental study by Park et al. [24] of the counterflow non-premixed laminar ethylene flames under DC electric fields is targeted as a benchmark. The counterflow burner consisted of two confronting nozzles with an exit diameter of $10\,\mathrm{mm}$. The separation distance between the two nozzles was fixed at $11\mathrm{mm}$. The C_2H_4/N_2 mixture was ejected from the lower nozzle, and the O_2/N_2 mixture was from the upper nozzle. The nozzle exit velocity was fixed at $20\,\mathrm{cm/s}$ to maintain a constant strain rate throughout the experiment. To remove the lateral diffusion by the ambient air, pure nitrogen was used as a shield flow and supplied through a concentric annular slot surrounding the nozzles. The velocity of the shield nitrogen was set at $20\,\mathrm{cm/s}$ to reduce the shear flow between the nozzle jet and the shield flow. Two metal perforated plates were placed at the exit planes of the nozzles. By being connected to the power supply unit, constant DC electric potentials were established on the two plates and roughly uniform electric fields were generated in the gap. The ground terminal from the power supply was always connected to the oxidiser side (the upper nozzle). Four typical experimental cases were selected for the simulation study, with different combinations of fuel/air compositions and high voltage supplies, shown in Table 2. The schematic of the counterflow burner nozzles and electrodes is shown in Fig. 3(a).The SF flames and SFO

flames are the fuel-rich and fuel-lean contourflow diffusion flames, respectively. The stagnation planes are closer to the fuel-side burner and oxidiser-side burner in the SF and SFO flames, respectively. Under the electric field of V_{dc} = $-2.0\,\mathrm{kV}$, the flame stagnation planes move downwards (see the photograph shots in Fig. 2(c)).

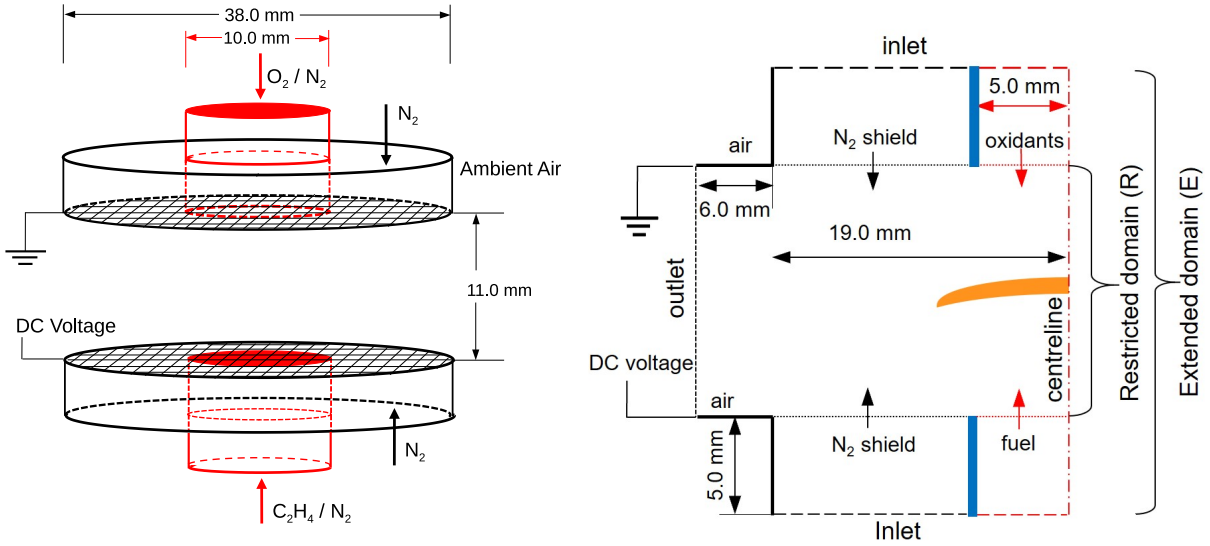

(a) Burner nozzles and electrodes

(b) Computational domains

Figure 1: The schematic of burner nozzles and electrodes of the counterflow flame and the computational domains.

Figure 3(b) depicts the axisymmetric computational domain for modelling the counterflow flame. Symmetry boundary conditions are applied along the flame centreline. The Dirichlet boundary conditions are applied at the two inflow / electrode cross-sections for velocity, species concentrations and electric potentials. The homogeneous Neumann boundary conditions are applied at the lateral outlet. Two different computational domains are considered in this work: one is a restricted domain (R) with the inlet and outlet set at two electrodes, in which the spatial grid includes 100×130 cells in the $z-r$ cylindrical coordinate system. The other one is the enlarged domain (E), with the inlet and outlet boundaries being extended $5\,\mathrm{mm}$ upstream of the electrode. The spatial grid of the extended domain (E) includes 140×130 cells. The simulation tests in the two different computational domains are presented in Section 4.1.

The time step for the simulation is set at 2×10^{-6} s. As the electric drift velocity of electrons is around 10-100 times larger than the ions, the time step for the transport equation of electrons is set at 1×10^{-7} s. In simulation, the flames initially develop in steady state, without modelling any external electric field or the soot formation. Then, the electric field and the soot model are included. Each simulation is then allowed to develop for the next $6\,\mathrm{ms}$ the flame stagnation plane does not continue to move [1].

[1] Some cases cannot reach to a steady state, especially for the soot formation cases with soot charging model but without the reduction by the electric factor on the soot process. Please see Fig. 6 (a) as an example.

Case	Compositions of Air/fuel		DC electric potential on the electrodes	
	lower nozzle $X(C_2H_2) : X(N_2)$	upper nozzle $X(O_2) : X(N_2)$	lower nozzle	upper nozzle
SFO	0.2: 0.8	1.0: 0.0	$-2.0\,\mathrm{kV}$	$0\,\mathrm{kV}$
SFO			$0\,\mathrm{kV}$	
SF	0.8: 0.2	0.2: 0.8	$-2.0\,\mathrm{kV}$	
SF			$0\,\mathrm{kV}$	

Table 2: Four different flames cases studied in the numerical modelling

3. Soot formation model in the electric field

In this section, we consider the models regarding nanoparticle formation under an electric field. Many research articles [56, 57] have discovered that aerosol particles can be induced to carry charges under an electric field, which definitely affect the trajectory of soot particles and the movement of the reacting fluid medium. Therefore, the particle charging model should be employed. At the moment, the population balance equation (PBE) is a classic macroscopic description for the dynamics and evolution of neutral nanoparticles. In this part, a second PBE will be added in order to calculate the emergence and dynamics of the charges on soot particles.

3.1. Polydisperse dynamics and electric charging of soot particles

Soot formation in the reacting flow is described by the population balance equation (PBE), given by

$$\frac{\partial n(v)}{\partial t} + \frac{\partial (u_i + V_i(v))n(v)}{\partial x_i} + \frac{\partial G n(v)}{\partial v} = \dot{B}\delta(v - v_0) + \frac{1}{2}\int_0^v \beta(v-w,w)n(v-w)n(w)\mathrm{d}w + \int_0^\infty \beta(v,w)n(v)n(w)\mathrm{d}w \tag{15}$$

where $n(v)$ [No./ $(\mathrm{m}^3 \cdot \mathrm{m}^3)$] is the particle number density at the particle size of v. G is the surface growth rate $[\mathrm{m}^3/\mathrm{s}]$, $\dot{B}$ is the nucleation rate [No./ $(\mathrm{m}^3 \cdot \mathrm{s})$] and v_0 is the nuclei volume $[\mathrm{m}^3]$ and β is the aggregation kernel. Under the electric field and in the weakly-ionised fluid, nanoparticles usually have a small amount of charges [56, 58]. The terms of Eq. 15 are the temporary change of number density, convection / diffusion, surface growth, nucleation, coagulation source and coagulation sink, respectively. By analogy with the drift velocity of ions (Eq. 9), the drift velocity of charged soot particles $V_i(v)$ is also composed of the diffusive velocity $K_i(v)$, thermophoretic velocity $U_i^{\mathrm{T}}(v)$ and the electrical mobility, presented as

$$V_i(v) = K_i(v) + U_i^{\mathrm{T}}(v) + E_i Q_{\mathrm{av}}(v)\mu(v) \tag{16}$$

the average number of charges $Q_{\mathrm{av}}(v) = \dfrac{Q_{\mathrm{p}}(v)}{n(v)}$ and its electrical mobility coefficient $\mu(v)$ is expressed in Table 1. For expressions of the diffusive velocity $K_i(v)$ and thermophoretic velocity $U_i^{\mathrm{T}}(v)$, readers are referred to in our previous work [40].

In fact, soot particles are transported in space according to Eq.15, with an velocity component $E_i Q_{\mathrm{av}}(v)\mu(v)$ induced by the electric force. Meanwhile, charges carried by the particles $Q_{\mathrm{p}}(v) = Q_{\mathrm{av}}(v)n(v)$ are also moving. Therefore, the spatial transport terms $\frac{\partial u_i \bullet}{\partial x_i}$ and $\frac{\partial V_i(v) \bullet}{\partial x_i}$ for $n(v)$ and $Q_{\mathrm{p}}(v)$ are identical [2]. As the growth term $\frac{\partial G \bullet}{\partial v}$ can be considered as the transport of particles in the size space, the growth term $\frac{\partial G \bullet}{\partial v}$ are also identical for $n(v)$ and $Q_{\mathrm{p}}(v)$. We assume that the nucleation process does not contribute charges to the soot particles. In the coagulation process, the charges on two particles will both settle on the formed large-size aggregate. In addition, under an electric field, soot particles are also induced to carry more charges [56], with a charging rate $\dot{C}(v)$ [C/($\mathrm{m}^3 \cdot \mathrm{m}^3$)], which will be discussed in Sec. 3.4. Therefore, the transport equation of charges on soot particles has been assembled as the following form

$$\frac{\partial Q_{\mathrm{p}}(v)}{\partial t} + \frac{\partial (u_i + V_i(v)) Q_{\mathrm{p}}(v)}{\partial x_i} + \frac{\partial G Q_{\mathrm{p}}(v)}{\partial v} = \dot{C}(v) \\ + \frac{1}{2}\int_0^v \beta(v-w,w) n(v-w) n(w) \left(\frac{Q_{\mathrm{p}}(v-w)}{n(v-w)} + \frac{Q_{\mathrm{p}}(w)}{n(w)} \right) \mathrm{d}w + \int_0^\infty \beta(v,w) Q_{\mathrm{p}}(v) n(w) \mathrm{d}w \tag{17}$$

The terms of Eq. 17 are the temporary change of particle charges, convection / diffusion, surface growth, soot charging, coagulation source and coagulation sink, respectively. Please note that Eq. 15 and Eq. 17 are interdependent descriptions on the spatial transport of charged particles, called two-equation PBE.

3.2. Common parameters of soot formation model

For soot formation in flames, the population balance equation (Eq. 15) governing the soot particle size distribution has been incorporated into the in-house CFD solver BOFFIN to model the polydisperse particulate phase in the multi-component reacting flow [40].

The processes of soot formation involve the nucleation modelled by the PAH dimerisation, surface growth modelled by the HACA mechanism with PAH condensation, and coagulation of spherical particles and fractal aggregates. This soot model has successfully predicted the soot formation in diffusion co-flow flames with fuels of ethylene [40], diesel and biodiesel surrogate [59], respectively. Empirical parameters for the nucleation rate $\dot{B}$, surface growth rate G, condensation rate (Eq. 15) and coagulation rate β are also listed in [40]. Based on experiments, soot particles are modelled as spherical nanoparticles if its size is smaller than $30.8\,\mathrm{nm}$ in diameter, otherwise, they are fractal aggregates composed of primary particles of $30.8\,\mathrm{nm}$ in diameter [60]. The sensitivity analysis of the nucleation and growth rates was in Ref. [40] on how these values affected the distribution of soot volume fraction in diffusion flames. The results showed that soot formation is very sensitive to the growth rate but not to the nucleation rate.

3.3. Empirical parameters for the nucleation and surface growth in the electric field

As flames without any electric field are also weakly ionised ($10^{15} - 10^{17}$ ions / m^3), the pathways of soot formation are known to be correlated with charged species. For example, under rich flame conditions, the reactions of aromatic

[2] A strict derivation should start from a control volume and the particles and the accompanying charges move into and out from its surface. Then the change of particles / charges in the control volume are expressed in the same differential form according to Gauss's Divergence Theorem.

precursor species (C_2H_2, C_3H_3), aromatics and soot particles are enhanced by ions, due to the high energy between an electronically excited molecule and a neutral species [52],

$$\mathrm{CH}\cdot + \mathrm{C_2H_2} \rightarrow \mathrm{C_3H_3}^+ + \mathrm{e}^- \tag{18a}$$

$$\mathrm{PAH} + \mathrm{C_3H_3}^+ \rightarrow \mathrm{PAH}^+ + \mathrm{C_3H_2} \tag{18b}$$

$$\mathrm{PAH} + \mathrm{CHO}^+ \rightarrow \mathrm{PAH}^+ + \mathrm{CO} \tag{18c}$$

$$\mathrm{C_3H_3}^+ + \mathrm{C_2H_2} \rightarrow \mathrm{PAH}^+ \tag{18d}$$

$$\mathrm{soot} \rightarrow \mathrm{soot}^+ + \mathrm{e}^- \tag{18e}$$

Bowal et al. [61] added easily ionised metals to flames and explored ionic aspects of soot formation. Enhanced interactions between the curved-PAHs (polar corannulene molecules) and K+ ions result in more rapid and abundant clustering, higher collision efficiencies, and longer cluster lifetimes, thus promoting the nucleation process at high temperatures.

Martin [62], however, summarised that the application of an electric field produces an ionic wind, leading to a negative influence on soot inception and growth. First of all, the accelerated chemi-ions in the flame entrain air in such a way that the flame is aerated, increasing oxidation and thereby reducing soot formation. Second, due to the ionic wind and the electric drift of charged soot particles, soot residence time in the flame was found to be reduced and the size of primary particles was significantly reduced. Last but more pronounced, the reaction zone is shifted in the electric filed, providing some quenching of the production of aromatics. Lawton and Weinberg [63] suggested that this reduces soot formation through the attachment of cations to soot particles.

$$\mathrm{soot} + \mathrm{C_3H_3}^+ \rightarrow \mathrm{soot}^+ + \mathrm{C_2H_2} + \mathrm{H} \tag{19}$$

Despite the insightful findings in the literature, quantitative information about the electric field effect on soot formation is scarce. The counterflow flame experiment [24] shows suppression effect of the electric field on the formation of soot and aromatic species, we therefore propose a simple empirical coefficient, relating the electric field intensities to the nucleation and growth rate,

$$C^{\mathrm{E}}(E_i) = \exp(-\gamma|E_i|) \tag{20a}$$

$$\text{or.} \qquad C_{\mathrm{E}}(E_i) = \exp(-\gamma|E_i|^2) \tag{20b}$$

The rates of nucleation and surface growth (including condensation rate) are thus corrected by the empirical coefficient,

$$\dot{B}^{\mathrm{E}} = (C^{\mathrm{E}})^2 \dot{B} \tag{21a}$$

$$G^{\mathrm{E}} = C^{\mathrm{E}} G \tag{21b}$$

The exponential form allows for a negligible effect on the soot formation if the electric field disappears while making the rates of nucleation and surface growth infinitely small if the electric intensity is extremely strong. An analysis of the functional forms and the γ value will be explored in Sec 4.3.

3.4. Soot charging model

Ambient aerosol particles are generally bipolar charged due to the random interaction between positive and negative ions with aerosols. Ionic charging of particles is usually described conceptually in terms of diffusion charging, for small particles or lower electric field, and field charging, for large particles or higher electric field. Long and Yao [64] summarised three categories of particle charging models used in the electrostatic ambience: a) the constant particle charge [65]; b) the particle charge is a function of time calculated based on the field / diffusion charging theory [66]; c) the particle charge rate is a function of time calculated based on the field / diffusion charging theory [56, 67]. Long and Yao [64] recommended that the model proposed by Lawless [56] should be the first choice relatively for numerical models of the particle dynamics in electrostatic precipitators. Here, this charging model is the combination of two charging process and the overall charging rate in dimensionless form, expresses as,

$$\frac{\mathrm{d}\nu}{\mathrm{d}\tau} = \begin{cases} f(\omega)\dfrac{\nu - 3\omega}{\exp(\nu - 3\omega) - 1} & \nu > 3\omega \\ \dfrac{3}{4}\omega\left(1 - \dfrac{\nu}{\omega}\right)^2 + f(\omega) & |\nu| \le 3\omega \\ \nu + f(\omega)\dfrac{-\nu - 3\omega}{\exp(-\nu - 3\omega) - 1} & \nu < -3\omega \end{cases} \tag{22}$$

$$f(\omega) = \begin{cases} (\omega + 0.475)^{-0.575} & \omega \ge 0.525 \\ 1 & \omega < 0.525 \end{cases} \tag{22a}$$

$$\nu = \frac{q_{\mathrm{p}} e}{2\pi\epsilon_0 d_{\mathrm{p}} k_{\mathrm{B}} T} \tag{22b}$$

$$\omega = \frac{\epsilon_{\mathrm{r}}}{\epsilon_{\mathrm{r}} + 2}\frac{E d_{\mathrm{p}} e}{k_{\mathrm{B}} T} \tag{22c}$$

$$\tau = \frac{\rho \mu_k}{\epsilon_0} t \tag{22d}$$

where ν is the dimensionless particle charge, ω is the dimensionless electric field intensity, τ is the dimensionless charging time. ϵ_{r} is the relative permittivity of the soot particle (ϵ_{r} = 12.0 for graphite). We take μ_k as the mobility coefficient of positive ions ($\mu_k = 1.0 \times 10^{-4}$ m / (m $\cdot$ V)).

Particle charging is thought to primarily influence the coagulation process by reducing the coagulation efficiency due to electrostatic repulsion, producing less aggregated primary particles that are more easily oxidised. The coagulation of charged particles β^{E} is formulated by considering a correction factor $\alpha_{v,w}^{l,m}$ on the coagulation kernel $\beta^{\mathrm{f/c}}$ in the free-molecular and continuum regime. Zheng et al. [57] has concluded that this charging model is effective for

aerosol particles with the diameter is larger than $2\,\mathrm{nm}$.

$$\beta^{\mathrm{E}}(v,w,l,m) = \beta^{\mathrm{f/c}}(v,w,l,m) \cdot \alpha_{v,w}^{l,m} \tag{23}$$

This correction factor is dependent on the discrete size pair v, w and charge pair l,m of particles [68–70]. It is calculated from electrostatic, image and ion induced Van der Waal forces due to charge on particles.

4. Results and discussion

4.1. Tests of chemical/ionic reactions of the flame without soot formation modelling in different computational domains

In this study, many assumed models, *.i.e.*, chemical/ionic reactions, soot formation and soot charging, have been incorporated and blended in order to replicate the counterflow sooting flame under an electric field. In the first step, we just show the simulated plasma flame without accounting the soot formation and charging models, shown by Figure 2, with a negative applied voltage $V_{\mathrm{dc}} = -2.0$ kV and under the baseline condition (without an electric voltage) for the left and right contour plots. Two different computational domains: the restricted domain R (Figure 2(a)) and the extended domain E (Figure 2(b)) are studied the effect on the simulation results. For each contour plot, distributions of two variables have been drawn: the OH mole fraction and the concentration of ions. As a comparison, Fig. 2(c) shows the flame stagnation plane, taken with a digital camera. The yellow luminosity is caused by black body radiation of soot particles, but also represents the flame characteristics in a sense. Therefore,in the simulation, the OH zone is very close to the combustion reaction zone and thus is used to represent the flame structure.

The photo (Fig. 2(c)) identifies a drastic visible variation of the flame stagnation plane, moving downward by $2.5\,\mathrm{mm}$ to the lower nozzle when a negative voltage $V_{\mathrm{dc}} = -2.0$ kV is applied, compared to the baseline condition. The flame still maintains a downward convex shape when it is moving. However, both simulations shows that the flame structure (demonstrated by the OH contour) has switched to being upward convex, with a negative voltage $V_{\mathrm{dc}} = -2.0$ kV applied. In addition, the predicted flame structures are slightly different in the two computational domains: First of all, when the electric filed ($V_{\mathrm{dc}} = -2.0\,\mathrm{kV}$) is applied, the flame kernel, predicted in domain R hardly ever budges, compared to the baseline case, while the flame edge moves downwards by around $2\,\mathrm{mm}$. In contrast, the prediction in domain E shows that the flame kernel drifts down by $0.86\,\mathrm{mm}$ under the negative voltage (V_{dc} = -2.0kV). Second, under the electric field, the downmost position (closest to the fuel burner) in domain R is on the flame edge while it is at around $r = 5\mathrm{mm}$ away from centreline in domain E. This is because positive ions are concentrated on the flame edge and at around $r = 5\mathrm{mm}$, according to the predictions in the two computational domains respectively, thus the flames are driven downward by the electric forces. As the change of flame stagnation (especially the flame kernel) plane towardsthe lower nozzle was identified at (V_{dc} = -2.0kV) in the images, the extended domain E is used for the following simulations.

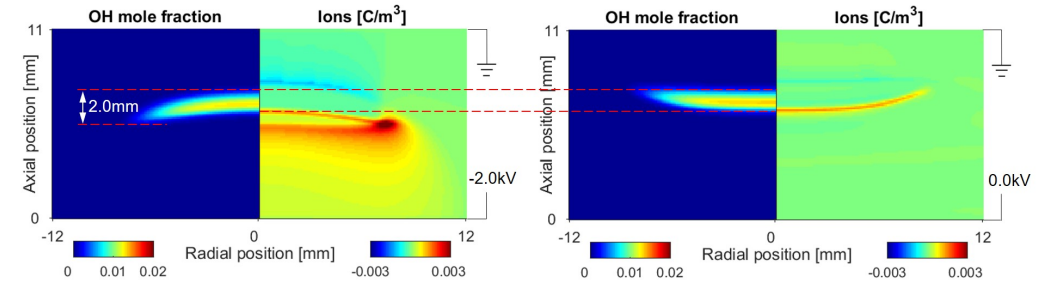

(a) Computational domain R (left: $V_{\mathrm{dc}} = -2.0\mathrm{kV}$; right: $V_{\mathrm{dc}} = 0.0kV$

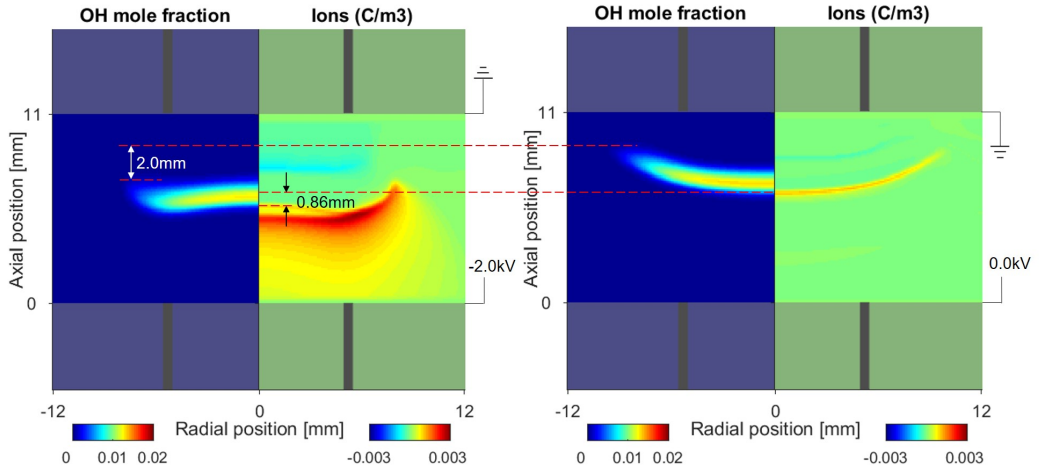

(b) Computational domain E (left: $V_{\mathrm{dc}} = -2.0\mathrm{kV}$; right: $V_{\mathrm{dc}} = 0.0kV$

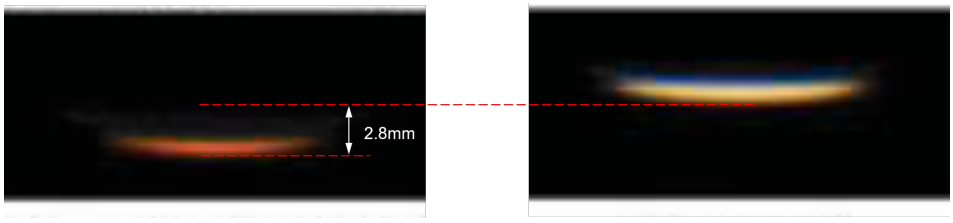

(c) Photographs of the flames in the experiment (left: $V_{\mathrm{dc}} = -2.0\mathrm{kV}$; right: $V_{\mathrm{dc}} = 0.0\mathrm{kV}$

Figure 2: Calculated OH mole fraction and distribution of ions of the SF (soot formation) flame with two different computational domains, compared with the photographs shot by a digital camera (Nikon, D700) in the experiment (data from [24] with permission from Taylor Francis ©).

Figure 3 displays the profiles of pressure gradient $-\frac{\mathrm{d}p}{\mathrm{d}t}$, electric body force E_zQ, electric intensity E_z, ion concentration Q and axial velocity V_z along the axial position using the computational domain E. Two axial lines are considered: $1.0\,\mathrm{mm}$ and $7.0\,\mathrm{mm}$ away from the centreline, corresponding to the flame centre and the flame edge, respectively. Two simulation cases are included: the SF flame in the negative electric field ($V_{\mathrm{dc}} = -2.0\mathrm{kV}$) and the baseline condition. As two explicit terms in the momentum equation (Eq. 5), the electric body force, as the driving power of the flow, is mainly counterbalanced by the pressure gradient. The joint effect of these two terms leads to a gradually stable movement of the flame structure in the electric field. The velocity and pressure are fixed on the boundary (the planes of electrodes), which will restrict the motion of the flame.

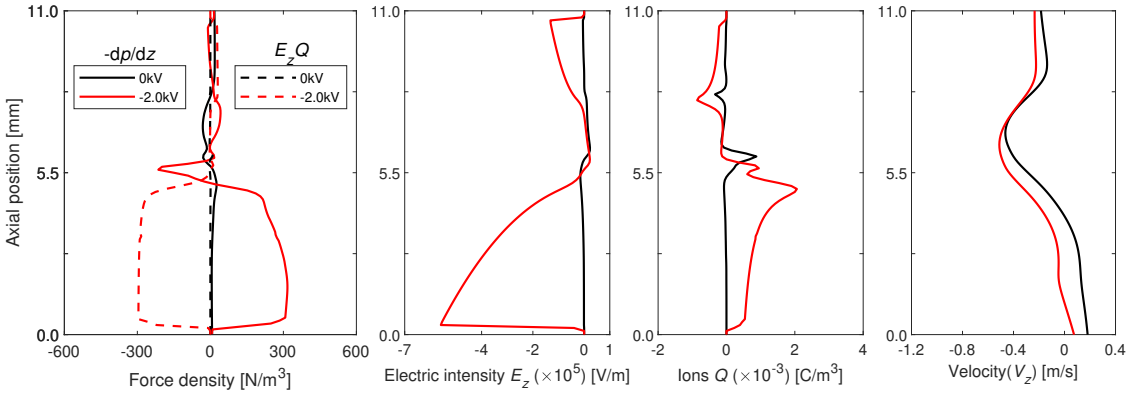

(a) $r = 1.0\mathrm{mm}$

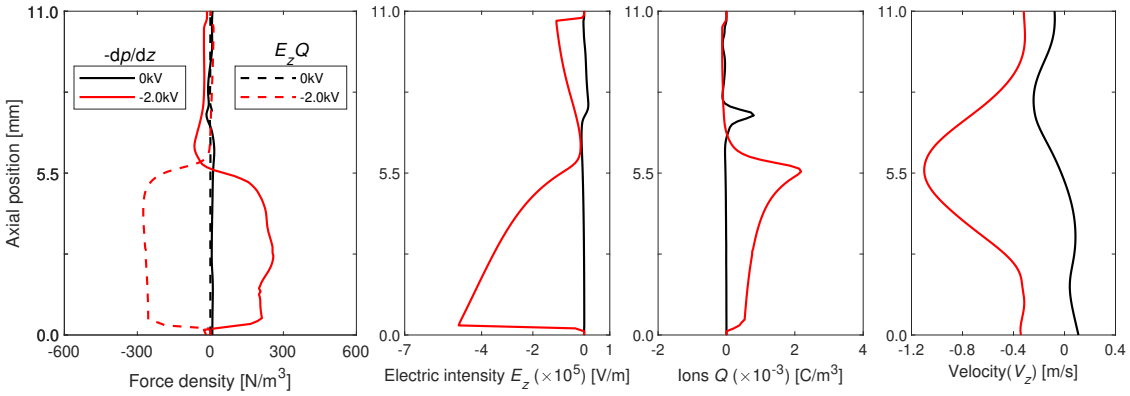

(b) $r = 7.0\mathrm{mm}$

Figure 3: Profiles of force density, electric intensity, ions concentration, and axial velocity along the axial position in three cases without soot modelling

There is an inconsistency of the flame stagnation plane between photo and the simulation without the soot formation model under a negative voltage. In the following sections, we consider the soot formation and particle charging models, together with the chemical/ionic reaction mechanism. We hope to achieve an upward convex flame plane as both the charges on soot particles and ions can be drifted under an electric field.

4.2. Simulations of sooting flames (SF) under an electric field with soot formation and particle charging models

In the last section, the predictions of the counterflow flames, excluding the soot formation (see Fig. 2), are unable to accurately capture the shape of the flame plane. In this section, we study how the soot formation and particle charging model affect the flame structure under an electric field. Particularly, if the particle charging model is considered, the spatial distribution of the electric charges will be modulated, thus larger electric forces will exert on the reaction fluid medium.

The experiment has measured the qualitative distribution of soot volume fraction (SVF), using planar laser induced incandescence (PLII) [71, 72], and the distributions of aromatic species and hydroxyl (OH) radicals, using laser induced fluorescence (PAH-LIF and OH-LIF) signals. Figure 4 (a-b) show the experimental laser signals the baseline condition and under a negative electric field ($V_{\rm dc} = -2.0$ kV) of the SF flames, respectively. For the baseline sooting flame, the main reaction zone of the OH radicals is located on the oxidiser side, soot particles and PAHs leak out radially along the streamlines of the counterflow geometry. Interestingly, by applying $V_{\rm dc} = -2.0{\rm kV}$, the soot particles were drastically reduced in the flames and the PLII signal could not be identified in Fig. 4(b). In addition, PAHs had a much weaker LIF intensity. The stagnation plane has moved towards the fuel nozzle, demonstrated by the stronger OH-LIF intensity.

In the simulation, we use the soot volume fraction and OH mole fraction to proportionally represent the PLII and OH-LIF signals. For the PAH-LIF signal, Lee et al. [6] reported that as the laser wavelength increases from $330\,{\rm nm}$ to $500\,{\rm nm}$, it indicates larger molecular sizes of the PAHs. Specially, Liu et al. [73] discovers that the small-size PAHs (*i.e.* naphthalene(A_2), Ethynylnaphthalene (A_2-CH_3)), large-size PAHs (*i.e.* coronene($C_{24}H_{12}$)), PAHs with five membered rings (*i.e.* cyclopenta pyrene ($C_{18}H_{10}$)) are responsible for the fluorescence located below $400\,{\rm nm}$, in the range $400\,{\rm nm}$ - $500\,{\rm nm}$ and the wavelength longer than $500\,{\rm nm}$, respectively. Herein, Park et al. [24] conducted the PAH-LIF measurements by selecting the central wavelength $450\,{\rm nm}$ in order to detect a discernible separation against the sooting zone (PLII signal). Accordingly, we should have modelled large-size gas-phase PAHs to correspond PAH-LIF signals, which however are not included in the chemistry [45]. In the simulation, we decide to use soot particle nascence ($d_{\rm p} < 2$ nm) to symbolise PAH-LIF signals.

Figure 4 (c) displays the quantitative distributions of the OH radicals, SVF and large-size PAHs in the baseline sooting flame. By comparing with the experimental counterpart in Figure 4 (a), the predictions of the flame structure and soot formation are in correct positions. However, the predicted PAHs show a wider distribution than the optical observation. Besides the soot formation model, the uncertainty of modelled PAH-LIF signals by using soot nascence also leads to this disparity.

Figure 4 (d-g) plots the simulation results of SF flames under the negative voltage $V_{\rm dc} = -2kV$, by adjusting two different modelling parameters: the soot particle charging model and the electric correction for the processes of nucleation and growth. If the particle charging model is not involved, as Fig. 4 (e) and (g) show, the flame stagnation plane is likely to crinkle as the reaction region around 6 - 7 mm away from the centerline sprints out downwards. The reason is similar to the flame plane in Fig. 2(b): more ions will concentrate on the flame edge if no charges are carried

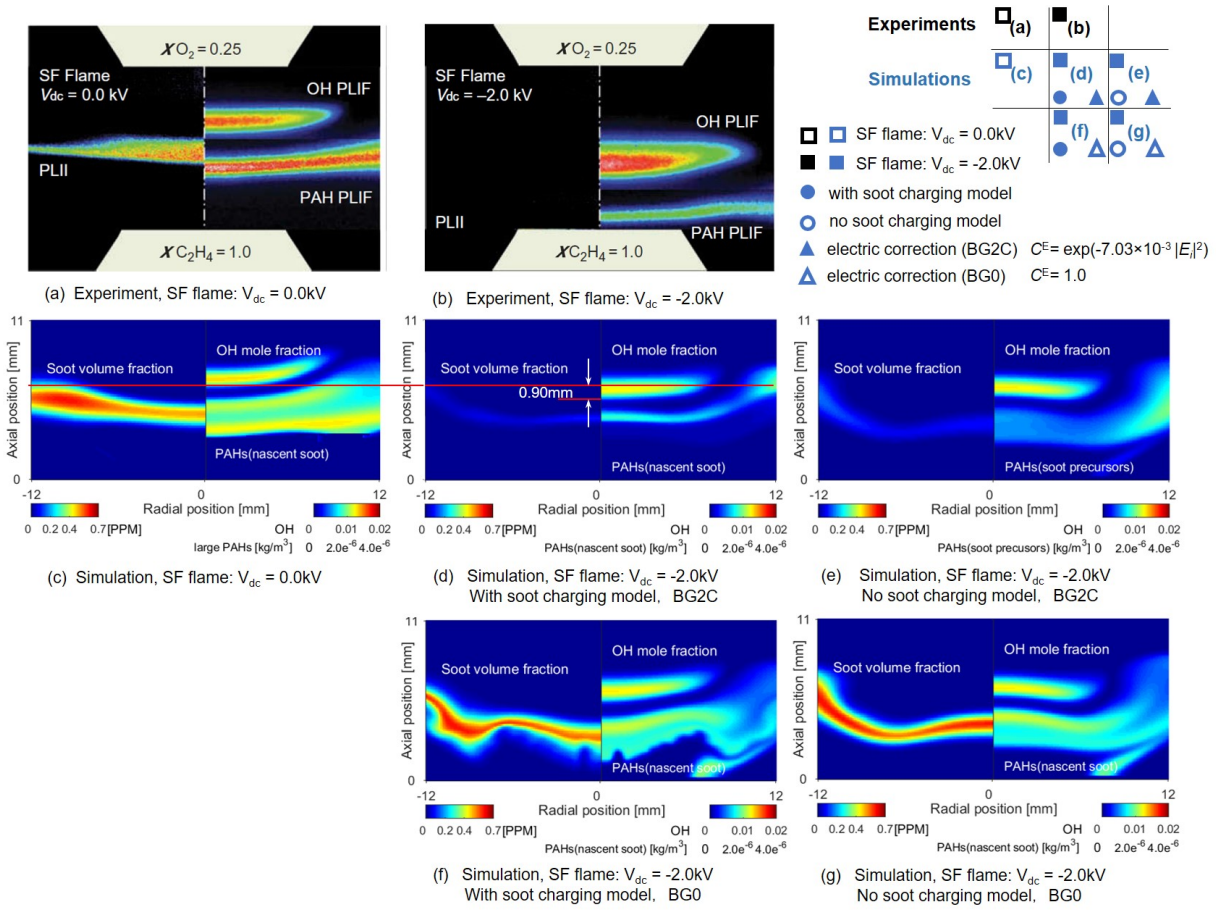

(a) Experiment, SF flame: V_{dc} = 0.0kV

(b) Experiment, SF flame: V_{dc} = -2.0kV

(c) Simulation, SF flame: V_{dc} = 0.0kV

(d) Simulation, SF flame: V_{dc} = -2.0kV
With soot charging model, BG2C

(e) Simulation, SF flame: V_{dc} = -2.0kV
No soot charging model, BG2C

(f) Simulation, SF flame: V_{dc} = -2.0kV
With soot charging model, BG0

(g) Simulation, SF flame: V_{dc} = -2.0kV
No soot charging model, BG0

Figure 4: Calculated distributions of the SVF, OH mole fraction and PAHs of the SF flames, regarding the application of the particle charging model and different correction factors C^{E}, compared with laser diagnostic measurements. (expermetnal data from [24] with permission from Taylor Francis ©)

by soot particles and an intensifier electric force exerts on the flame edge than the flame kernel.

If the nucleation and growth processes are not corrected in the electric field BG0: $C^{\mathrm{E}} = 1.0$), the prediction of Fig. 4 (f) and (g) shows no clear evidence of a decline in soot formation. Therefore, the modification of the flow field and reaction zone only by the ionic wind are not able to heavily suppress soot.

Even if soot charging model is considered, charged soot particles are expelled by the electric field with a slower rate than their formation and growth. That is to say, the most important cause of the soot suppression by the electric field is on chemical aspect, that is, the chemical reactions of soot nucleation and surface growth are significantly inhibited by the external electric field. In this research, we therefore employed a simple correction factor (Eq. 20) on the processes of nucleation and surface growth. As a result, we achieved a satisfying result in Fig. 4 (d). Herein, we find that the flame stagnation plane (represented by the SVF and PAHs) has remained unperturbed in the simulation duration ($6\,\mathrm{ms}$), in contrast to huge or minor perturbations in other simulation cases. The flame stagnation plane (represented by the OH mole fraction) in Fig. 4 (d) has moved downwards for around $1\,\mathrm{mm}$, despite still a shorter distance than $2.5\,\mathrm{mm}$ in the laser measurement. The SVF is also adjusted extremely weak as expected. Although the modelled PAH-LIF signal shows the weaker intensity as observed in the measurement under the negative voltage, it fails to replicate the significant modification of its measured spatial distribution toward the fuel nozzle. The reason will be explored in Sec. 4.5.

4.3. Parametric study of the correction factor for the nucleation and growth

An application of the correction factor C^{E} makes a significant difference to the prediction of the sooting flame with the charging model under an external electric field, depicted by Figs. 4 (d) and (f). The flame stagnation plane is not unsteady or crimped any longer. Moreover, the SVF and the concentration of PAHs (soot precursors) have indeed declined a lot. In this section, the correction factor is varied to analyse its effect on soot formation and the gas mixture. Two functional forms are considered: Eq. 20a and Eq. 20b, called the exponential linear form (BG1) and exponential square form (BG2) in the following paragraphs. Three correction coefficients are listed in Table 3 for each functional form: 1/5, 1/10, 1/20 if the average electric field intensity is equal to $-2.0\mathrm{kV}/11\mathrm{mm} = 1.8 \times 10^5\mathrm{kV}/\mathrm{m}$, marked as BG1A, BG1B, BG1C,taking the exponential linear form as an example.

No consideration		$\mathrm{C}^{\mathrm{E}}(E_i) = \exp(-\gamma\lvert E_i\rvert)$			$\mathrm{C}^{\mathrm{E}}(E_i) = \exp(-\gamma\lvert E_i\rvert^2)$		
mark	expression	mark	γ	value of C_{E} when $E_i = 1.8 \times 10^5$V/m	mark	γ	value of C_{E} when $E_i = 1.8 \times 10^5$V/m
BG0	$\mathrm{C}^{\mathrm{E}} = 1.0$	BG1A	-8.85×10^{-6}	0.2	BG2A	-3.77×10^{-3}	0.2
		BG1B	-1.27×10^{-5}	0.1	BG2B	-5.40×10^{-3}	0.1
		BG1C	-1.65×10^{-5}	0.05	BG2C	-7.03×10^{-3}	0.05

Table 3: Correction factors of nucleation and growth rates of soot formation in the electric fields tested in Fig. 5

Axial profiles of six variables, including the local correction factor, electric intensity, nucleation rate, surface growth rate, condensation rate and the SVF, are shown in Fig. 5. Here we focus on two radial positions: r =

$1.0\,\mathrm{mm}$ and r = $7.3\,\mathrm{mm}$, representing the central region and the flame edge, respectively. And we also find unsteady perturbations on the edge in certain simulation cases.

As a whole, we can observe that the profiles of the correction factor and electric intensity can be divided into two parts by the region of soot formation, around 4 - $5\,\mathrm{mm}$ above the lower burner (fuel side). On the upper burner side (oxidiser side), the electric intensity is negligible so that the correction factor is close to zero. In contrast, on the lower burner side, the electric intensity is much larger than the average value $1.8 \times 10^5 \mathrm{kV/m}$, where the rates of nucleation, surface growth and condensation are suppressed, compared to the BG0 case (without electric correction $C^{\mathrm{E}} = 1.0$), thus the declined SVF. As the correction factor is reduced, from BG1A to BG1C, or from BG2A to BG2C, the SVF declines and the region of soot shrinks, accompanied by the decreasing rates of soot formation processes.

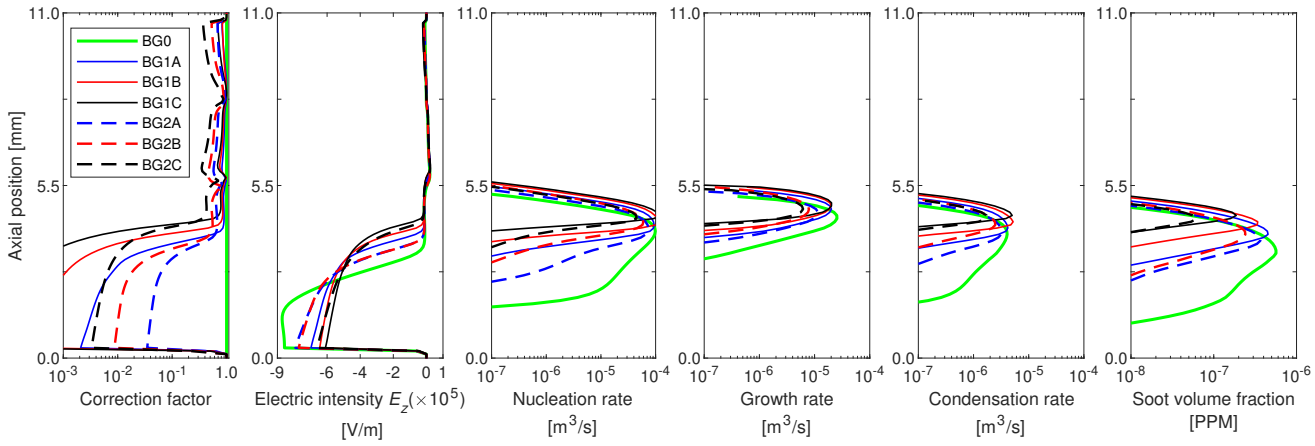

(a) r = 1.0 mm

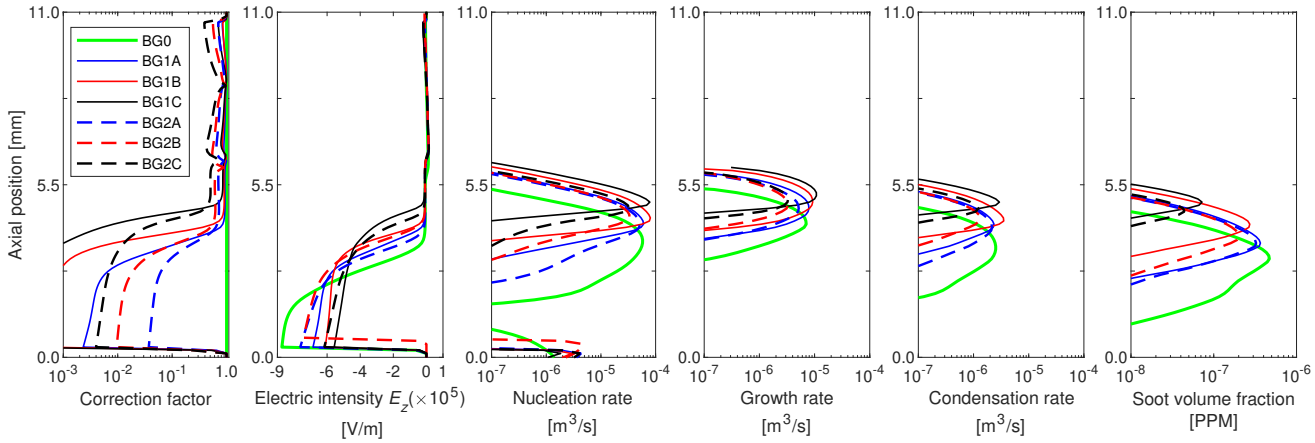

(b) r = 7.3 mm

Figure 5: Axial profiles of variables soot formation (with the charging model) regarding different correction factors C^{E} in the SF flame under an electric field ($V = -2.0\mathrm{kV}$)

Interestingly, we focus on the modulation effect of the two functional forms Eq. 20a and Eq. 20b. On the fuel side, the correction factor of the exponential linear form (BG1) is larger than the exponential square form (BG2) while

the BG2 factor is slightly larger on the oxidiser side. The smoother profiles of BG2 factors determine a wider range of soot formation, which makes steeper gradients of the electric intensity on the fuel burner side because the charges on soot particles modulates the electric field.

Another question arises that how we should coordinate the soot particle charging model and the electric correction factor in order to achieve a physical prediction of the flame structure and soot formation. As we have predicted satisfying distributions of laser diagnostic signals in the case BG2C (see Fig. 4(d)), contours plots of ions and soot particles charges of the BG2 group are shown, in Fig. 6.

When the particle charging process is not considered in Fig. 6 (e), a layer of positive ions occurs to balance the electric neutrality in the flame under an electric field. It can be understood that the electrons (major negative charges) are electrically driven with a much faster speed than other ionic species (see Table 1). On the other hand, when we include the particle charging model Fig. 6 (a - d), soot particles are positively charged, as evidenced in many experimental research [74]. In the given time period ($5\,\mathrm{ms}$), the amount of positives charges on soot particles has exceeded the ionic species. In fact, the ionic concentration decreases compared with the case without the particle charging process, to reach a new balance of electric neutrality with soot charges.

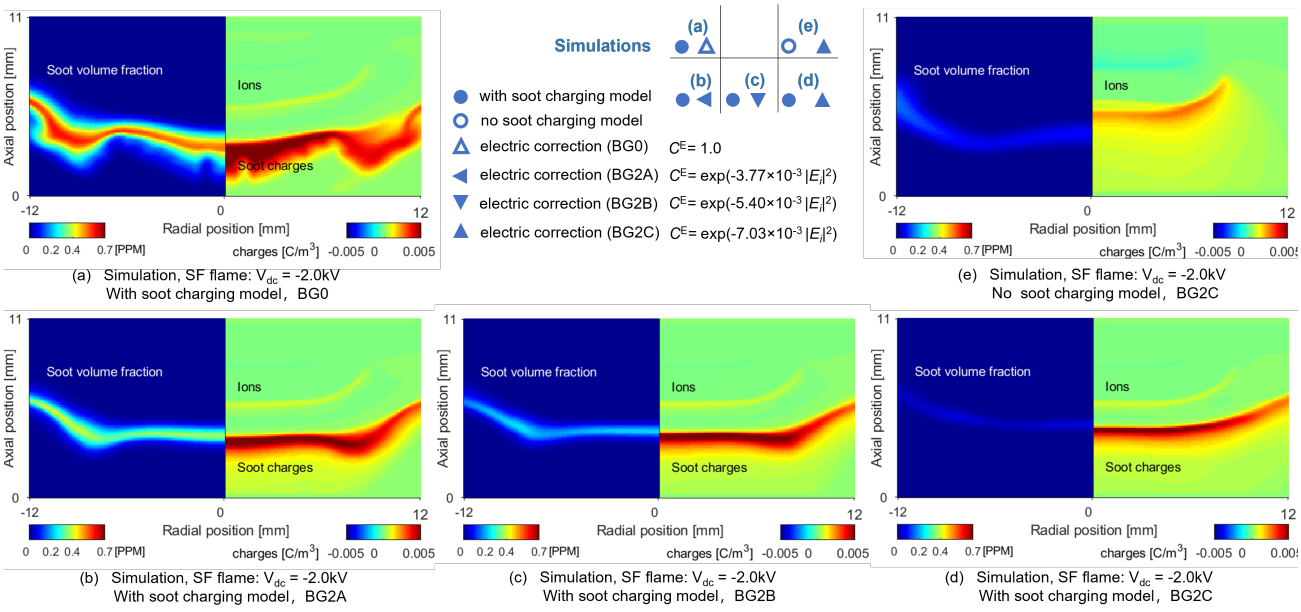

Figure 6: Calculated distributions of the SVF, OH mole fraction and and of the SF (soot formation) flames, using different values of the correction factor C^{E}

In Fig. 6 (a), it is found that a large amount of soot charges induces a drastic perturbation on the region of soot formation, while the ion layer keeps steady. As the effect of the correction factor is gradually enhanced (from BG1A to BG1C, see Fig. 6 (b-d)), accompanied by an evident decline of the SVF, the amount of soot charges slightly decreases. This leads to an improved stability in the region of soot formation, and thus the flame structure. It is also credibly estimated that the average number of charges on a unit volume of soot increases with an enhanced correction

factor, by quantitatively comparing the SVF and soot charges.

4.4. *Effects of the critical charging diameter in the particle charging model*

In this research, we have assumed that only particles larger than $2\,\mathrm{nm}$ are able to become charged. However, smaller charged soot particles were also observed as the resolution of particle mass analysers improved [75]. Fig. 7 compare the predictions on the sooting flames using different critical charging diameters in the particle charging model (BG2C): $dc_{\mathrm{cr}} = 2\,\mathrm{nm}$ and $dc_{\mathrm{cr}} = 0.5\,\mathrm{nm}$. It is observed that steady distributions of soot formation and charges still remain when the critical charging diameter is adjusted smaller. More subtly, the soot volume fraction slightly decreases in contrast to the accumulating soot charges in the case of $dc_{\mathrm{cr}} = 0.5\,\mathrm{nm}$. This is because soot precursors in the size range $0.5\,\mathrm{nm} < d_{\mathrm{p}} < 2\,\mathrm{nm}$ are able to be charged, leading to a reduction of the residence time of these charged nascent soot in the flame.

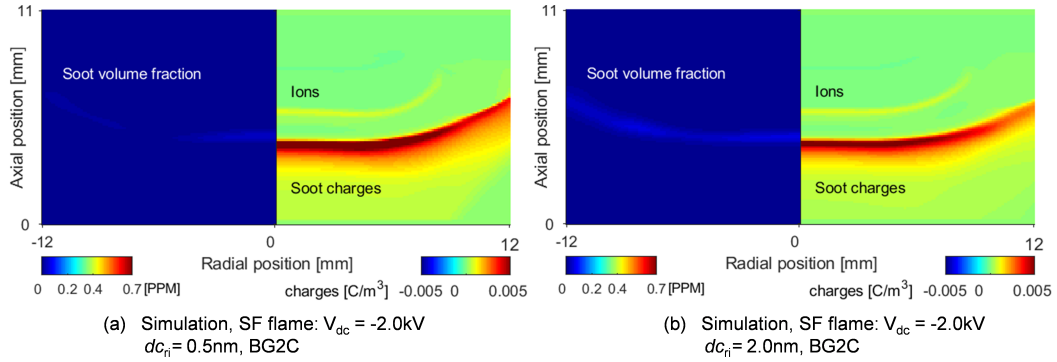

Figure 7: Calculated distributions of the SVF, OH mole fraction and PAHs of the SF (soot formation) flames, using different critical diameters in the particle charging model

Figure 8 displays the distribution of particle number at the position of the maximum SVF and the distribution of particle charges at the position of the maximum concentration of particle charges at the radial location r = 1 mm. The graphs consolidate the conclusions drawn from Fig. 6 and Fig. 7. As the electric correction factor is intensified, (from BG0 to BG2A, to BG2C), the number of soot particles and particle charges decreases. If the critical size for particle charging is reduced (*.i.e* dc_{cr} from $2\,\mathrm{nm}$ to $0.5\,\mathrm{nm}$), charges on nascent particles sharply increases (2 - 3 orders of magnitude greater than on the particles with $dc_{\mathrm{p}} > 2\,\mathrm{nm}$). As the nascent particles are of a higher electric mobility (see Table 1), they are easily driven away by the electric field thus the residence time of nascent particles is shortened. This in fact suppresses the growth of particles. Therefore, the number of large-size particles and the charges on them synchronously decrease.

4.5. *Modelling of PAH-LIF signals using different species*

Now, we look into the models of PAH-LIF signals. According to Sec 4.2, different sizes of PAH molecules and clusters can fluoresce in different intensity, leading to the complexity of decomposing the PAH-PLIF signal. In this

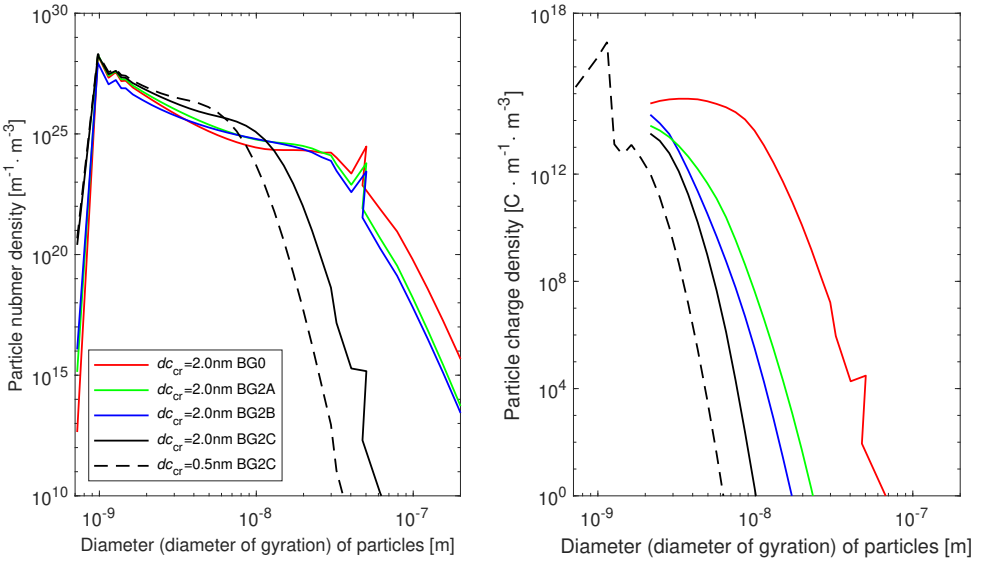

(a) Distribution of particle number at the position of maximum SVF

(b) Distribution of particle charge at the position of maximum concentration of charges

Figure 8: Distributions of the particle number and the particle charge at particular locations of r = 1 mm

paper, we used nascent soot particle ($d_{\mathrm{p}} < 2\,\mathrm{nm}$) to symbolise PAH-LIF. However, what would happen if we choose to use the small-size PAH molecules from the chemistry set?

Figure 9 compares the two modelling approaches for the PAH-LIF signals. Herein, two sooting flame conditions are studied, corresponding to the baseline case and $V_{\mathrm{dc}} = -2.0\,\mathrm{kV}$ in Figs. 4 (a) and (b). The first approach is the mass concentrations of the gas PAH molecules contributing to the soot nucleation [60], including naphthalene A_2, acenaphthylene A_3 and pyrene A_4. The second approach is expressed by the nascent soot particles, as in Sec 4.2. They are depicted on the two sides of each image with respect to the centreline of the burner. The gas-molecule modelled PAH-LIF signal intensifies a lot under the negative voltage, which is opposite to the measurement and the nascent soot modelled signal. This is because the correction factor (*i.e.* BG2C) is introduced to consider the effect of an electric field on the nanoparticle formation, the rates of nucleation, surface growth and condensation are modulated diminished, thus reducing the consumption of PAH molecules. This, as a result, leads to an accumulation of PAH molecules.

The root cause for reverse tendencies by the two PAH-LIF modelling appraoches is attributed to the chemistry set under the electric field. The ionic reactions [46] were simply implanted on the chemical mechanism [45]. The variation of the chemical reactions (especially the PAH pathways) in the strong electric field and plasma ambient is not considered. To compensate, the electric correction factor is introduced to manually adjust the chemical processes during nanoparticle formation.

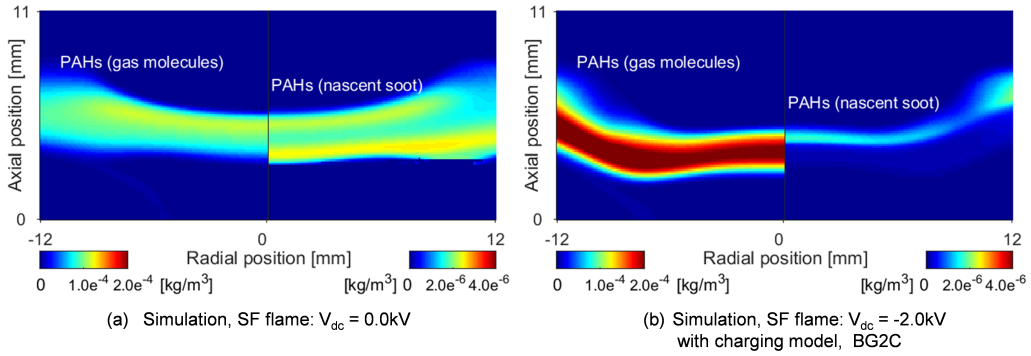

Figure 9: Calculated distributions of PAHs in the SF flames, regarding using different PAH-LIF modelling means

4.6. Multi-condition tests of soot formation / oxidisation flames (SFO) under an electric field

To test the generality of the model for soot formation in flames under an electric field, the modelling framework is applied to soot formation / oxidisation (SFO) flames.The parameters of mobility on the first line of Table 1 and electric factor for the nucleation and surface growth BG2C are also used in this section. Figure 10 compares the predicted spatial distributions of the soot particles, PAHs, and OH radicals with the original measurements. The images in the upper row correspond to the SFO baseline flame without any electric field and the SFO flame with a negative voltage $V_{\mathrm{dc}} = -2.0\,\mathrm{kV}$, and the images in the lower row are their simulation results.

The SFO baseline flame in Fig. 10(a) contains a vast distribution of OH radicals and a relatively small number of soot particles due to the oxidative structure of the flame. The soot particles are fully oxidised within the reaction zone, and the level of PAHs is significantly smaller than in the SF flame (see Fig. 4(a)). All the details are basically captured by the simulation shown in Fig. 10(c).

Under the DC electric field, OH-PLIF intensity becomes stronger, and its distribution is wider and has drifted towards the fuel burner side (see Fig. 10(b)). These modifications are reflected by the simulation in Fig. 10(d) , yet less obviously. The prediction also accurately replicates the disappearance of soot formation (PLII signal) and PAHs, despite an insignificant level of PAH-PLIF intensity in the measurement.

5. Conclusions

In this article, we proposed a comprehensive PBE-CFD modelling framework to investigate the effect of an external electric field on the soot formation of a non-premixed ethylene flame in a counterflow burner. The framework, integrating the population balance equation (PBE) with a reactive flow solver for the multi-component ideal gases, has been enhanced to include various electric effects. An ion mechanism used in both fuel-rich and fuel-lean combustion is combined with a detailed chemistry for neutral gaseous species and small-molecule aromatics to retain the full chemistry. As the formed nanoparticles carry charges in the electric field, a second PBE of the transport of particle charges has been added, accompanying the original PBE of the particle number density. This is the first attempt so far

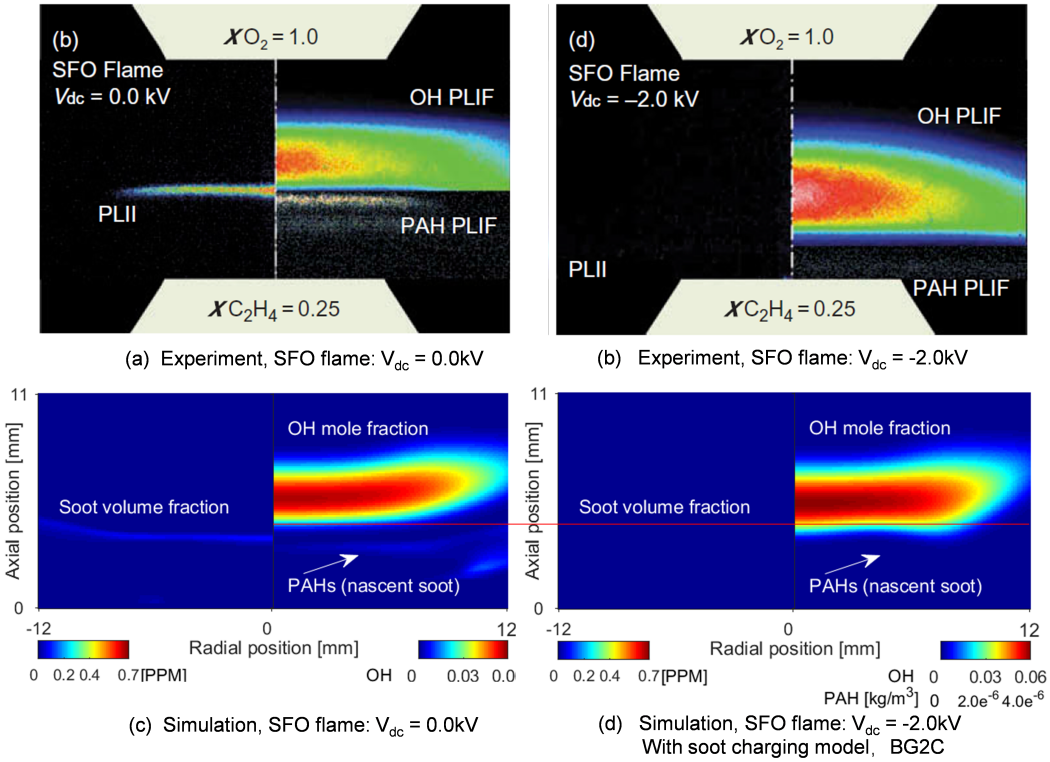

Figure 10: Calculated distributions of the SVF, OH mole fraction and PAHs of the SFO flames (data from [24] with permission from Taylor Francis ©)

to formulate a two-PBE model to the describe the evolution of charged particles and analyse its effect on the reactive fluid medium. The electric force for the gas mixture is included in the momentum equations. The electric drift velocities for ions and soot particles are also considered in the transport equations of ions and the PBE of charged soot particles, respectively.

The simulations have shown that the presence of the electric field changes the stagnation plane of the counterflow flames and reduces the soot formation in both fuel-rich and fuel-lean conditions. The application of the soot particle charging model, accompanied by a proper electric correction factor on the nanoparticle processes of nucleation and surface growth, significantly helps to achieve a stable flame structure in the simulation. The introduction of the electric correction factor reveals that the suppression of soot formation in an electric field is mainly caused by the inhibited chemical reactions of the PAH nucleation and particle surface growth, which is more important than the electric drift of the charged particles. Reducing the critical size of the particle charging process enhances the electric drift of nascent soot, thus lessening its subsequent evolution. Altogether, the coupled two-equation PBE-CFD framewor using the electric mobility parameters in Table 1 and the electric factor for soot formation process, has reproduced the movement of the flame stagnation plane and the suppression of soot formation observed in the experiment.

Owing to the complexity and importance of electric field effects on soot or nanoparticle formation, further numerical and experimental studies in the field are warranted. Firstly, many parameters in this electric-charging PBE-CFD model, *.i.e* the mobility of ionic species, electrons and charge particles (Table 1), the coefficient of coagulation for charged particles, and the particle charging model, need to be studied in greater details. Second, this study models the effect of an electric field on the flames and soot formation only from a macroscopic viewpoint, *.i.e*, by introducing the electric correction factor to approximate the atomistic mechanisms of particle nucleation and surface reactions under an electric field. It is desirable to look into the mesoscopic and molecular aspects of the relevant phenomena. Work has already started in the molecular dynamics studies of the PAH formation, nucleation and nanoparticle surface reactions [76–79], further research will focus on the effect of an external electric field on these processes of soot formation with the aid of molecular dynamics modelling. Recently, a combination of reactive force field and electron force field (eFF) molecular dynamics simulations has been constructed to reveal the fundamental mechanisms for the influence of the electric field on ethanol oxidation reactions at atomic and subatomic scales [80]. An extension of the method can potentially include soot dynamics, which will provide unprecedented insight and data to aid modelling of electric field effects on sooting flames.

Appendix A Validation of the chemi-ionisation and the electric current in a methane-air premixed flame

The chemi-ionisation mechanism and the electric field model are validated in a one-dimensional burner-stablised methane-air premixed flame. The ionised flame was studied experimentally under an external electric field by Peerlings et al. [81]. Speelman et al. [35] presented a model to simulate the electric field behaviour and to predict the electric currents in these flames. The equivalence ratios tested were between 0.6 to 1.2 and the saturation current was

found dependent on the equivalence ratio. To validate the chemi-ionisation mechanism, the mathematical model for the electric potential and the electric transport of ionic species, we reproduce the simulation of Speelman et al. [35] at the equivalence ratio $\phi = 1.0$. The computational domain in this study is represented schematically in Figure A.1. The fuel/air mixture enters with a prescribed mass flow rate and temperature through the burner deck, which is situated at x = 0 and is grounded. The ionisation electrode is located at $x = L$.

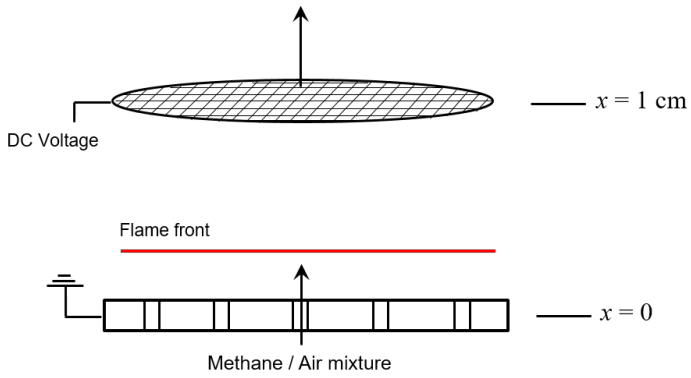

Figure A.1: Schematic of the burner and the electrodes by Peerlings et al. [81]

Figure A.2 shows the profiles of temperature and neutral species concentrations from the simulations of Speelman et al. [35] and this work. Although Speelman et al. [35] used GRI-Mech 3.0 [82] to model the neutral species chemistry while the chemical mechanism by Blanquart et al. [45] are used in this work, the distributions of temperatures and major species are in good agreement.

Figure A.3 compares the concentrations of major charged species (H_3O^+ and electrons) in the premixed flame, without an applied electric field in the two simulations. As Speelman et al. [35] employed the three-step ion mechanism of [33] but the present simulation applied a multi-step ion mechanism of [29], the concentrations of H_3O^+ and electrons in this prediction are about 70% of the results by Speelman et al. [35]. This is acceptable when different ion mechanisms are employed.

Figure A.4 compares the current densities caused by the cations and anions (including electrons), $J+$ and $J-$ from the simulations of Speelman et al. [35] and this work, respectively, as the applied positive potential is increased. With an external electric field, both simulations show the negative value of $J-$ downstream of the reaction zone, which means that the electrons are moving towards the electrodes at x = $1.0\,\mathrm{cm}$ while the negative value of $J-$ at x = 0 implies that the cations are moving towards the electrode at the burner upstream of the flame front. Both simulations also show that at $\Delta V_{\mathrm{dc}} = 20\,\mathrm{V}$ when the electric current is not saturated, the positive $J+$ has been found because the gradient of the ion concentration is negative and the mass diffusion and bulk velocity of the flow in the positive direction overwhelm the electric transport of cations in the negative direction. This work also shows that as the electric voltage increases, the negative electric current density increases until that it reaches a saturation current

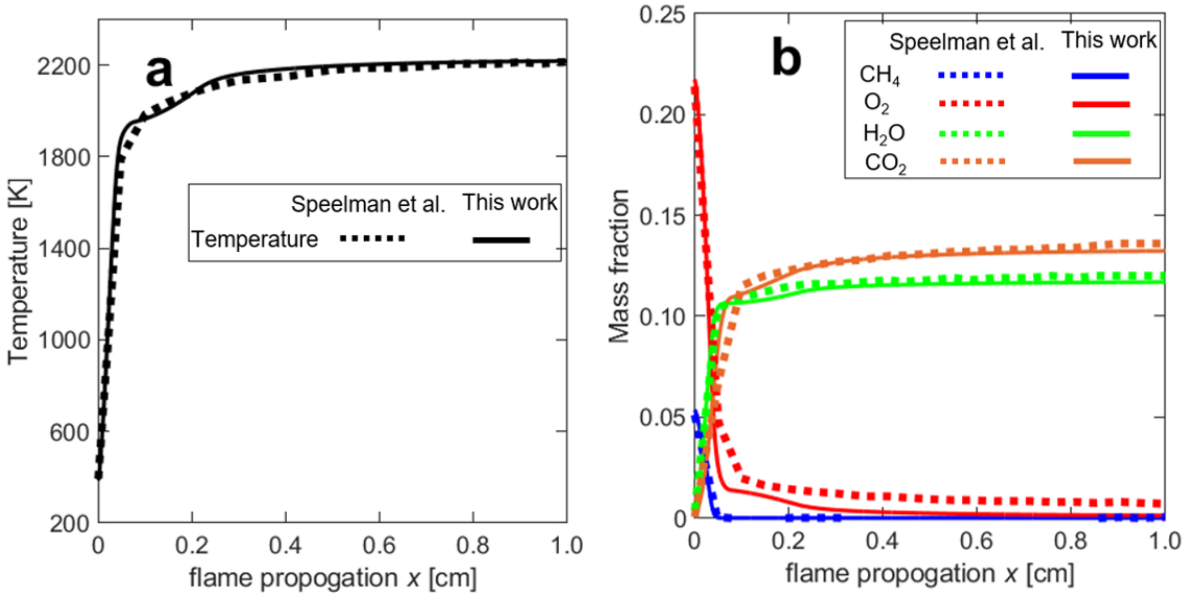

(a) Temperature profile

(b) Major species mass fraction

Figure A.2: Comparison of distributions of temperature and the major species mass fraction at $V_{dc} = 0V$ between the simulations by Speelman et al. [35] and in this work

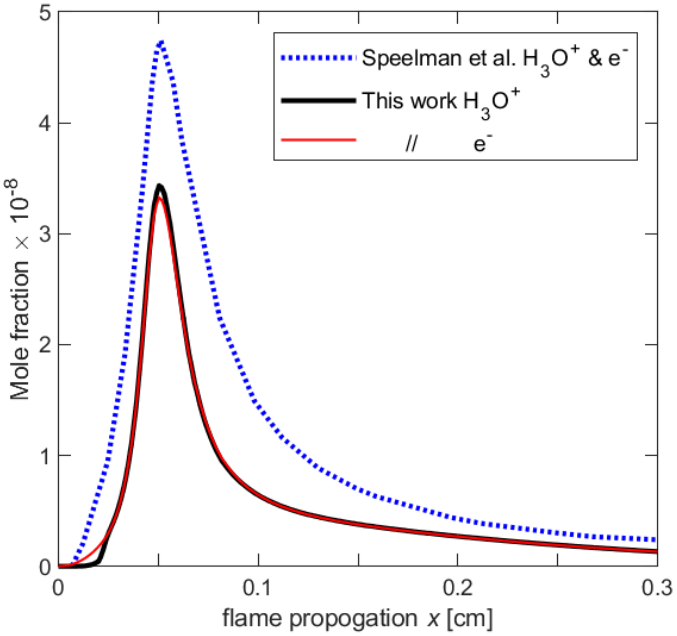

.

Figure A.3: Comparison of mole fractions of hydronium (H_3O^+) and elections at $V_{dc} = 0V$ from the simulations by Speelman et al. [35] and this work

at $\Delta V_{\mathrm{dc}} = 80$V. The major difference is that the absolute value of the electric current density in this work is smaller than Speelman et al. [35] (at $\Delta V_{\mathrm{dc}} = 20\,\mathrm{V}$). This is because the peak values of the mole fraction of ions and electrons in this work are smaller than those of Speelman et al. [35] and the distributions of ions and electrons (the gradient of concentrations of ions and electrons) are different in these two simulations, shown in Fig. A.3.

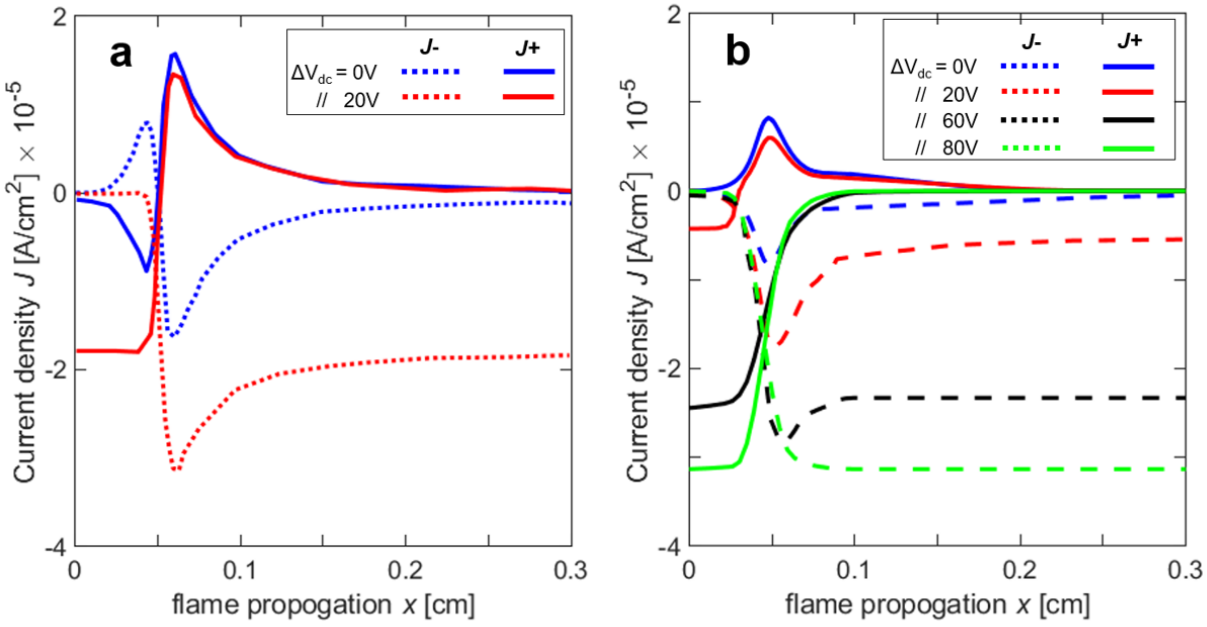

(a) Speelman et al. [35]

(b) This work

Figure A.4: Comparison of current densities by cations and anions (electrons) from the simulations by Speelman et al. [35] and in this work

Figure A.5 displays the electric current as a function the applied electric potential the equivalence ratio $\phi = 1.0$. We can find that Speelman et al. [35]'s model and the present model predict the current saturation at 50V and 80V, respectively. However, both electric potentials for current saturations are smaller than 120V, which was measured in the experiment. In addition, Speelman et al. [35]'s model and the present model have overpredicted the measured saturation current by a factor of 2.5 and 1.7, respectively. The main reason that the saturation current in this work is smaller than the results by Speelman et al. [35] is that the concentrations of ions and electrons in the present model using the chemi-ionisation mechanism of Chen et al. [29] are predicted smaller than those of Speelman et al. [35] using the mechanism of Belhi et al. [33].

As a summary, validations have been conducted in a one-dimensional burner-stablised methane-air premixed flame under a DC electric field [81]. The saturation voltage is captured and the current-voltage curves are qualitatively

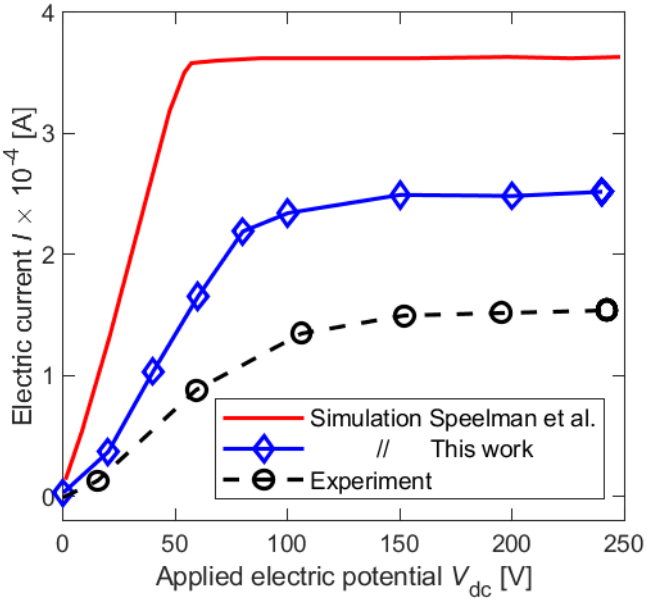

.

Figure A.5: Comparison of electric currents as a function the applied electric potential obtained by the model of Speelman et al. [35] and the present model

correct, which has confirmed the effectiveness of the present model of the electric field and the electric transport of cations and anions. In addition, the results imply that the mobility of the ions and electrons and the chemi-ionisation rate are qualitatively reasonable. The discrepancies are mainly due to the differences in the chemi-ionsation mechanisms used by Speelman et al. [35] and the present studies, respectively.

Acknowledgements

Funding for the research provided by the UK Engineering and Physical Sciences Research Council (EPSRC) under Grant Nos. EP/S012559/1 and EP/R029598/1 is gratefully acknowledged. K.H. Luo would like to express heartfelt gratitude to Prof Ken Bray for his inspiration and guidance in combustion research.

References

[1] M. V. Tran, M. S. Cha, Time evolution of propagating nonpremixed flames in a counterflow, annular slot burner under ac electric fields, Proceeding of the Combustion Institute 36 (2017) 1421–1430.

[2] S. H. Won, S. K. Ryu, M. K. Kim, M. S. Cha, S. H. Chung, Effect of electric fields on the propagation speed of tribrachial flames in coflow jets, Combustion and Flame 152 (2008) 496–506.

[3] J. D. B. J. van den Boom, A. A. Konnov, A. M. H. H. Verhasselt, V. N. Kornilov, L. P. H. der Goey, H. Nijmeijer, The effect of a DC electric field on the laminar burning velocity of premixed methane/air flames, Proceeding of the Combustion Institute 32 (2009) 1237–1244.

[4] S. Marcum, B. Ganguly, Electric-field-induced flame speed modification, Combustion and Flame 143 (2005) 27–36.

[5] Y. Ju, S. O. Macheret, M. N. Shneider, R. B. Miles, Numerical study of the effect of microwave discharge on the premixed methane-air flame, in: AIAA/ASME/SAE/ASEE Joint Propolsion Conference and Exhibit, Florida, USA, 2004.

[6] S. M. Lee, S. S. Yoon, C. S. H., Synergistic effect on soot formation in counterflow diffusion flames of ethylene-propane mixtures with benzene addition, Combustion and Flame 136 (2004) 493–500.

[7] A. Ata, J. S. Cowart, A. Vranos, B. M. Cetegen, Effects of direct current electric field on the blowoff characteristics of bluff-body stabilized conical premixed flames, Combustion Science and Technology 177 (2005) 1291–1304.

[8] E. Sher, A. Pokryvailo, E. Jacobson, M. Mond, Extinction of flames in a nonuniform electric field, Combustion Science and Technology 87 (1992) 59–67.

[9] E. Sher, G. Pinhasi, A. Pokryvailo, R. Bar-on, Extinction of pool flames by means of a DC electric field, Combustion and Flame 94 (1993) 244–252.

[10] A. Cessou, E. Varea, K. Criner, G. Godard, P. Vervisch, Simutaneous measurements of oh, mixture fraction and velocity fields to investigate flame stabilisation enhancement by electric field, Experiments in Fluids 52 (2012) 905–914.

[11] H. Duan, X. M. Wu, C. Zhang, Y. C. Cui, J. C. Hou, C. Li, Z. Q. Gao, Experimental study of lean premixed $CH_4/N_2/O_2$ flames under high-frequency alternating-current electric fields, Energy & Fluids 29 (2015) 7601–7611.

[12] M. K. Kim, H. S. Chung, H. H. Kim, Effect of AC electric fields on the stabilization of premixed bunsen flames, Proceedings of the Combustion Institute 33 (2011) 1137–1144.

[13] X. Yuan, Effects of AC electric field on small laminar nonpremixed flames, Ph.D. thesis, King Abdullah University of Science and Technology, Kingdom of Saudi Arabia, 2015.

[14] D. C. Murphy, M. Sánchez-Sanz, C. Fernandez-Pello, The role of non-thermal electrons in flame acceleration, Combustion and Flame 182 (2017) 48–57.

[15] G. T. Kalghatgi, Spark ignition, early flame development and cyclic variation in I. C. engines (1987) 149–161.

[16] A. C. DeFilippo, Microwave-assisted ignition for improved internal combustion engine efficiency, Ph.D. thesis, University of California, Berkeley, USA, 2013.

[17] I. Ganesh, R. Johnson, G. V. N. Rao, Y. R. Mahajana, S. S. Madavendra, B. M. Reddy, Microwave-assisted combustion synthesis of nanocrystalline $MgAl_2O_4$ spinel powder, Ceramics International 31 (2005) 67–74.

[18] M. Venkatesh, G. Suresh Kumar, S. Viji, S. Karthi, E. K. Girija, Microwave assisted combustion synthesis and characterization of nickel ferrite nanoplatelets, Modern Electronic Materials 2 (2016) 74–78.

[19] A. Y. Starikovskii, Plasma supported combustion, Proceedings of the Combustion Institute 30 (2005) 2405–2417.

[20] J. B. Michael, T. L. Chng, R. B. Miles, Sustained propagation of ultra-lean methane/air flames with pulsed microwave energy deposition, Combustion and Flame 160 (2013) 796–807.

[21] M. Kono, K. Iinuma, S. Kumagai, The effect of DC to 10 MHz electric field on flame luminosity and carbon formation, Proceedings of the Combustion Institute 18 (1981) 1167–1174.

[22] M. Kono, F. B. Carleton, F. J. Weinberg, The effect of nonsteady electric fields on sooting flames, Combustion and Flame 78 (1989) 357–364.

[23] L. Xie, T. Kishi, M. Kono, Investigation on the effect of electric fields on soot formation and flame structure of diffusion flames, Proceedings of the Combustion Institute 24 (1992) 1059–1066.

[24] D. G. Park, B. C. Choi, M. S. Cha, S. H. Chung, Soot reduction under DC electric fields in counterflow non-premixed laminar ethylene flames, Combustion Science and Technology 186 (2014) 644–656.

[25] M. S. Cha, S. M. Lee, K. T. Kim, S. H. Chung, Soot suppression by nonthermal plasma in coflow jet diffusion flames using a dielectric barrier discharge, Combustion and Flame 141 (2005) 448–447.

[26] M. Saito, T. Arai, M. Arai, Control of soot emitted from acetylene diffusion flames by applying an electric field, Combustion and Flame 119 (1999) 356–366.

[27] N. G. J. Wang, Y., Z. T. Alwahabi, K. D. King, K. Ho, Q. Ya, Effect of a uniform electric field on soot in laminar premixed ethylene/air flames, Combustion and Flame 157 (2010) 1308–1315.

[28] A. Sayed-Kassem, P. Gillon, M. Idir, V. Gilard, On the effect of a dc electric field on soot particles' emission of a laminar diffusion flame, Combustion Science and Technology (2019).

[29] B. J. Chen, H. Y. Wang, Z. D. Wang, J. Han, A. B. S. Alquaity, H. Wnag, N. Hansen, S. M. Sarathy, Ion chemistry in premixed rich methane flames, Combustion and Flame 202 (2019) 208–218.

[30] C. Van Gulijk, J. C. M. Marijnissen, M. Makkee, J. A. Moulijn, A. Schmidt-Ott, Measuring diesel soot with a scanning mobility particle sizer and an electrical low-pressure impactor: Performance assessment with a model for fractal-like agglomerates, Combustion Science and Technology 35 (2004) 633–655.

[31] M. J. Papac, D. Dunn-Rankin, Modelling electric field driven convection in small combustion plasmas and surrounding gases, Combustion Theory and Modelling 12 (2008) 23–44.

[32] K. Yamashita, S. Karnaniand, D. Dunn-Rankin, Numerical prediction of ion current from a small methane jet flame, Combustion and Flame 156 (2009) 1227–1233.

[33] M. Belhi, P. Domingo, P. Vervisch, Direct numerical simulation of the effect of an electric field on flame stability, Combustion and Flame 157 (2009) 2286–2297.

[34] M. Belhi, P. Domingo, P. Vervisch, Modelling of the effect of DC and AC electric fields on the stability of a lifted diffusion methane/air flame, Combustion Theory and Modelling 17 (2013) 749–787.

[35] N. Speelman, L. de Goey, J. van Oijen, Development of a numerical model for the electric current in burner-stabilised methane–air flames, Combustion Theory and Modelling 19 (2015) 159–187.

[36] M. Belhi, B. J. Lee, F. Bisetti, H. G. Im, A computational study of the effects of dc electric fields on non-premixed counterflow methane-air flames, Journal of Physics D: Applied Physics 50 (2017) 494005.

[37] B. S. Chen, A. L. Garner, S. P. M. Bane, Simulation of flame speed enhancement of a hydrocarbon flame with a microwave field, Combustion and Flame 207 (2019) 250–264.

[38] F. Bisetti, M. E. Morsli, Calculation and analysis of the mobility and diffusion coefficient of thermal electrons in methane/air premixed flames, Combustion and Flame 159 (2013) 3518–3521.

[39] S. B. Dworkin, Q. Zhang, M. J. Thomson, N. A. Slavinskaya, U. Riedel, Application of an enhanced PAH growth model to soot formation in a laminar coflow ethylene/air diffusion flame, Combustion and Flame 158 (2011) 1682–1695.

[40] A. X. Liu, C. E. Garcia, F. Sewerin, B. A. O. William, S. Rigopoulos, Population balance modelling and laser diagnostic validation of soot particle evolution in laminar ethylene diffusion flames, Combustion and Flame (2020).

[41] E. Y. K. Yee, Numerical Simulation of Soot in Laminar Flames, Ph.D. thesis, University of Cambridge, UK, 2016.

[42] F. A. Williams, Elementary derivation of the multicomponent diffusion equation, American Journal of Physics 26 (1958) 467–469.

[43] T. Pedersen, R. C. Brown, Simulation of electric field effects in premixed methane flames, Combustion and Flame 94 (1993) 433–448.

[44] A. Kronenburg, R. W. Bilger, J. H. Kent, Modelling soot formation in turbulent methane–air jet diffusion flames. combustion and flame, Combustion and Flame 121 (2000) 24–40.

[45] G. Blanquart, P. Pepiot-Desjardins, H. Pitsch, Chemical mechanism for high temperature combustion of engine relevant fuels with emphasis on soot precursors, Combustion and Flame 156 (2009) 588–607.

[46] J. Prager, U. Riedel, J. Warnatz, Modeling ion chemistry and charged species diffusion in lean methane–oxygen flames, Proceedings of the Combustion Institute 31 (2007) 1129–1137.

[47] H. R. Jones, A. N. Hayhurst, Measurements of the concentrations of positive and negative ions along premixed fuel-rich flames of methane and oxygen, Combustion and Flame 166 (2016) 86–97.

[48] Theory Manual: Chemkin-Pro for Reaction Design, San Diego, 2008.

[49] J. L. Delcroix, Physique des Plasmas I, Monographies DUNOD, 1963.

[50] J. Han, M. Belhi, F. Bisetti, Numerical modelling of ion transport in flames, Combustion Theory and Modelling 19 (2015) 744–772.

[51] S. Selle, U. Riedel, Heat and Mass Transfer under Plasma Conditions, The New York Academy of Sciences, 1999.

[52] A. B. Fialkov, Investigations on ions in flames 23 (1997) 399–528.

[53] W. Sutherland, A dynamical theory of diffusion for nonelectrolytes and the molecular mass of albumin, Philosophical Magazine 9 (1905) 781–785.

[54] J. Vinogradov, E. Sher, I. Rutkevich, M. Mond, Voltage-current characteristics of a flame-assisted unipolar corona 127 (2001) 2041–2050.

[55] R. T. Nishida, Measuring Aerosol Nanoparticles by Ultraviolet Photoionisation, Ph.D. thesis, University of Cambridge, U. K., 2015.

[56] P. A. Lawless, Particle charging bounds, symmetry relations, and an analytic charging rate model for the continuum regime. journal of aerosol science, Journal of Aerosol Science 27 (1996) 191–215.

[57] C. H. Zheng, X. F. Zhang, Z. D. Yang, C. S. Liang, Y. S. Guo, Y. Wang, x. Gao, Numerical simulation of corona discharge and particle transport behavior with the particle space charge effect, Journal of Aerosol Science 118 (2018) 22–33.

[58] B. Y. H. Liu, A. Kapadia, Combined field and diffusion charging of aerosol particles in the continuum regime., Journal of Aerosol Science 9 (1978) 227–242.

[59] B. Tian, A. X. Liu, C. T. Chong, L. M. Fan, S. Ni, J. H. Ng, S. Rigopoulos, K. H. Luo, S. Hochgreb, Experimental and numerical study on soot formation in laminar diffusion flames of biodiesels and methyl esters, Proceedings of the Combustion Institute (2020).

[60] A. X. Liu, S. Rigopoulos, A conservative method for solution of the population balance equation, and application to soot formation, Combustion and Flame 205 (2019) 506–521.

[61] K. Bowal, J. W. Martin, A. J. Misquitta, M. Kraft, Ion-induced soot nucleation using a new potential for curved aromatics, Combustion Science and Technology 191 (2019) 747–765.

[62] J. W. Martin, Investigating the role of curvature on the formation and thermal transformations of soot, Ph.D. thesis, University of Cambridge, UK, 2020.

[63] J. Lawton, F. Weinberg, Electrical aspects of combustion, Clarendon Press, 1969.

[64] Z. Long, Q. Yao, Evaluation of various particle charging models for simulating particle dynamics in electrostatic precipitators, Journal of Aerosol Science 41 (2010) 702–718.

[65] H. J. White, Particle charging in electrostatic precipitation, Transactions of the American Institute of Electrical Engineers 70 (1951) 1186–1191.

[66] R. Cochet, Lois charge des fines particules (submicroniques) etudes théoriques—controles récents spectre de particules, Colloque International la Physique des Forces Electrostatiques et Leurs Application 102 (1951) 1186–1191.

[67] W. B. Smith, J. R. McDonald, Development of a theory for the charging of particles by unipolar ions, Journal of Aerosol Science 7 (1976) 151–166.

[68] H. J. Mick, A. H. P. Roth, Computer simulation of soot particle coagulation in low pressure flames, Journal of Aerosol Science 22 (1991) 831–841.

[69] L. Laakso, J. M. Mäkelä, L. Prijola, M. Kulmala, Development of a theory for the charging of particles by unipolar ions, Journal of Aerosol Science 7 (1976) 151–166.

[70] K. Ghosh, M. Joshi, Y. S. Mayya, A. Khan, B. K. Sapra, Modeling studies on coagulation of charged particles and comparison with experiments, Journal of Aerosol Science 105 (2017) 35–47.

[71] P. Roth, A. V. Filippov, In situ ultrafine particle sizing by a combination of pulsed laser heatup and particle thermal emission, Journal of Aerosol Science 27 (1996) 95–104.

[72] B. F. Kock, C. Kayan, J. Knipping, H. R. Orthner, P. Roth, Comparison of LII and TEM sizing during synthesis of iron particle chains, Proceedings of the Combustion Institute 30 (2005) 1689–1697.

[73] P. Liu, Z. W. He, H. G. L., B. Guan, The diagnostics of laser-induced fluorescence (LIF) spectra of PAHs in flame with TD-DFT: special focus on five-membered ring, The journal of physical chemistry A 119 (2015) 13009–13017.

[74] M. M. Maricq, Size and change of soot particles in rich premixed ethylene flame, Combustion and Flame 137 (2004) 340–350.

[75] T. Baum, S. Löffler, P. Löffler, P. Weilmünster, K. H. Homann, Fullerene ions and their relation to PAH and soot in low-pressure hydrocarbon flames, Berichte der Bunsengesellschaft für physikalische Chemie 96 (1992) 841–857.

[76] H. Wang, K. Wen, X. Q. You, Q. Mao, K. H. Luo, M. Pilling, S. Robertson, Energy transfer in intermolecular collisions of polycyclic aromatic hydrocarbons with bath gases he and ar, The Journal of Chemical Physics 151 (2019) 044301.

[77] Q. Mao, K. H. Luo, Trace metal assisted polycyclic aromatic hydrocarbons fragmentation, growth and soot nucleation, Proceedings of the Combustion Institute 37 (2019) 1023–1030.

[78] Q. Mao, D. Hou, K. H. Luo, X. Q. You, Dimerization of polycyclic aromatic hydrocarbon molecules and radicals under flame conditions, Journal of Physical Chemistry A 122 (2018) 8701–8708.

[79] Q. Mao, A. C. T. van Duin, K. H. Luo, Formation of incipient soot particles from polycyclic aromatic hydrocarbons: A reaxff molecular dynamics study, Carbon 121 (2017) 8701–8708.

[80] X. Z. Jiang, K. H. Luo, Reactive and electron force field molecular dynamics simulations of electric field assisted ethanol oxidation reactions, Proceedings of the Combustion Institute 38 (2020).

[81] L. Peerlings, M. Manohar, V. Kornilov, L. de Goey, Flame ion generation rate as a measure of the flame thermo-acoustic response, Combustion and Flame 160 (2013) 2490–2496.

[82] G. P. Smith, D. M. Golden, N. W. Moriarty, B. Eiteneer, M. Goldenberg, C. T. Bowman, R. K. Hanson, S. Song, W. C. Gardiner Jr, V. V. Lissianski, Z. Qin, GRI-Mech 3.0, ???? URL: http://combustion.berkeley.edu/gri-mech/version30/text30.html.